CHAPTER 2

THEORETICAL BACKGROUND

This chapter focus on the critical reviews of the theories and the backgrounds which mainly related to the electrochemical energy storage base on carbon, metal oxide especially the nickel oxide and conducting polymer. Additionally, the rechargeable batteries and the characterization theories involving the experiment were presented below:

2.1 Electrochemical energy storage

Electrochemical energy storage devices consist of the three main categories such as supercapacitors, rechargeable batteries and fuel cells [41-43]. Supercapacitor store and release the energy by charging/discharging of the electrons and ions in the electrochemical system based on the electrostatic double layer or via redox activities. Unlike the batteries and the fuel cells, they deliver electrical energy by the conversion of chemical energy. The difference between supercapacitors and batteries was explained as follow.

2.1.1 Supercapacitor

Supercapacitors or electrochemical capacitors or ultracapacitors are one of electrochemical energy storage devices, which have the construction like the batteries. It comprises of the active materials including carbonaceous material, some transition metal oxides (MnO_2, RuO_2) and conducting polymers on the conductive current collector, separator, and electrolyte solution. As shown in Figure 2.1, it is seen that when the voltage is applied across two conductive current collectors, the electrons and ions in the electrolyte solution will move toward the opposite charging electrodes, leading to the charge separation and accumulation on the electrode surface (charging process). Then the energy can be released when discharging method occur.

1) Basic of supercapacitors [44]

Base on the mechanism, the supercapacitors can be divided into two main types including electrical double layer capacitors (EDLCs) and pseudocapacitors. The EDLCs storage/release energy through the pure electrostatic charge adsorption/desorption at the interface between the electrode and electrolyte solution under the applied voltage without a presence of chemical reaction. The pseudocapacitance keeps the energy via the fast and reversible redox activities at the interface between the electrode and electrolyte.

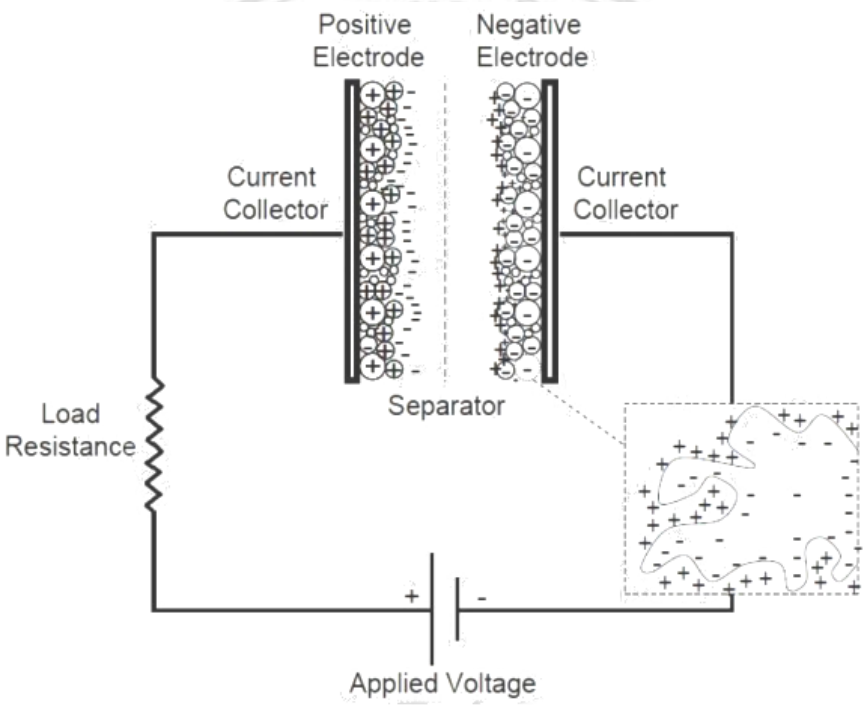

Figure 2.1 Schematic diagram of a supercapacitor device [45]

1.1) Electrical Double Layer capacitors (EDLCs)

This type storage energy base on the electric double layer (also named as Helmholtz double layer), which is formed at the interface between electrode/electrolyte. The combination of several theoretical models by many researchers used to explain the electric double layer. The first model was elucidated by Helmholtz in 1853. He explored the distribution of the opposite charge at the interface of the colloidal particles as shown in Figure 2.2 (a). The Helmholtz model mentioned about the two layers, which is formed at the interface by the opposite charges, leading to the construction of an electric double layers, comprising one layer at the surface of

electrode and the other layer in the electrolyte solution [46] with the thickness of an atom range (~5-10 Aº).

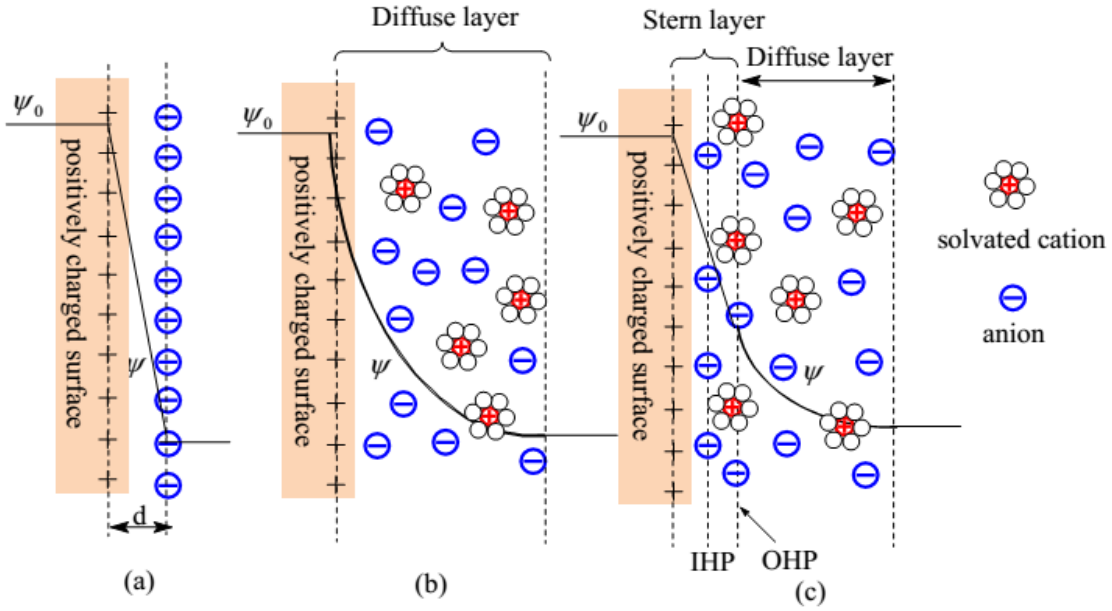

Figure 2.2 Models of the electrical double layer; (a) the Helmholtz model, (b) the Gouy-Chapman model, and (c) the Stern model. The OHP. IHP, d, ψ_0 and ψ are inner Helmholmz plane, outer Helmholtz plane, the double layer thickness/distance, the potential at the surface of the electrode and the potential at the interface of electrode/electrolyte, respectively [47].

This simple model had a pattern like the two conductive electrodes of capacitors. Later, in 1910 and 1913 Gouy and Chapman developed this model by considering a continuous distribution of anions and cations in the electrolyte solution; known as diffusion layer (in Figure 2.2 (b)). However, the model had the weakness about the overestimation of the capacitance close to the surface of the electrode. The capacitance value result came from the mathematical model of Chapman about the diffusion layer which used to elucidate the ion distribution in the electrolyte solution. Because they assumed that the ions were point charge, leading to finding an error in potential profile. In 1924, Stern developed the Gouy-Chapman model by integration the Helmholtz model. Moreover, he studied about the size of ion and molecule of the electrolyte and also give details about the total capacitance, relating to the electric double layer. Thus, Stern model had two ion distribution regions as shown in Figure 2.2 (c). The first was Stern layer of which contained the specific ion (inner Helmholtz plane; IHP) and non-

specifically adsorbed counterions (outer Helmholtz plane; OHP). The other was diffusion layer which defined as Gouy-Chapman model.

Considering the potential (ψ_0, ψ) variation relates to the electric double layer structure in Stern model (Figure 2.2 (c)), it is observed that the potential distribution of both compact layer is linear. But they have a different slope. It also examines the changing of the potential distribution from the linearity in the diffuse layer region reaching to the minimum potential. After that, the value becomes constant in the bulk solution region, due to the rapid mobility of ions [44]. The bulk solution located next to the diffusion region, which not shown in Figure 2.2. The total capacitance of the electrostatic double layer, according to Stern model can be achieved as followed equation [48];

$$\frac{1}{C_{dl}} = \frac{1}{C_H} + \frac{1}{C_{diff}} \tag{2.1}$$

In which C_{dl}, C_H and C_{diff} was total capacitance, the capacitance of Stern layer and capacitance of diffusion layer. Thus, from equation 2.1 it is seen that the overall capacitance is come from the capacitance at Stern layer region combine with the capacitance at diffusion region. However, the overall model assumed by using the planar surface electrode. Hence, the porous and the high surface area materials, which are used generally in the EDLCs applications should have more complex model than this.

To understand the EDLCs supercapacitor, it usually compares with the conventional dielectric capacitor [49]. The construction of conventional capacitor vs. the EDLCs capacitor is shown again in Figure 2.3.

In Figure 2.3, it is shown that the conventional capacitors and EDLCs capacitors have the common features, which are the components of the devices, consisting of the positive electrode, negative electrode and the medium. However, general medium, which is widely used in the conventional capacitor is the dielectric materials or non-conductive solution such as mica, paper, paraffin, mineral oil etc. [47, 49]. When the potential is applied, the dipoles in the medium will be polarized and generated the electric charge (Q) between the interface of the electrode and the medium. In contrast, the medium of the EDLCs capacitors is the electrolyte solution of which is a liquid or

solid ionic conductor [49]. In the EDLCs capacitor under the applying of the voltage across the electrodes, the electric charge storage by the accumulation of ions at the electrode/electrolyte, which occurs on both of electrode. Thus, the difference between medium leading to the capacitance value for conventional capacitors, and EDLCs supercapacitors are in a uF range and mF range, respectively. The relation between capacitance, electric charge and applied voltage can be written as equation 2.2;

$$C = \frac{Q}{V} = \frac{\varepsilon_0 \varepsilon_r}{d} A \tag{2.2}$$

Where C is capacitance, Q is among f charge storage, V is applied voltage. Moreover, for dielectric capacitance $\varepsilon_0, \varepsilon_r$, A, d is the vacuum permittivity (8.854 x 10^{-12} F/m), the dielectric constant, the area of the electrode and the distance between two conductive plates. For the EDLCs supercapacitor the ε_r, A, d is the electrolyte dielectric constant, A (m^2/g) is the specific surface area of the electrode accessible to the electrolyte ions, and d (m) is the thickness of the electric double layer, respective.

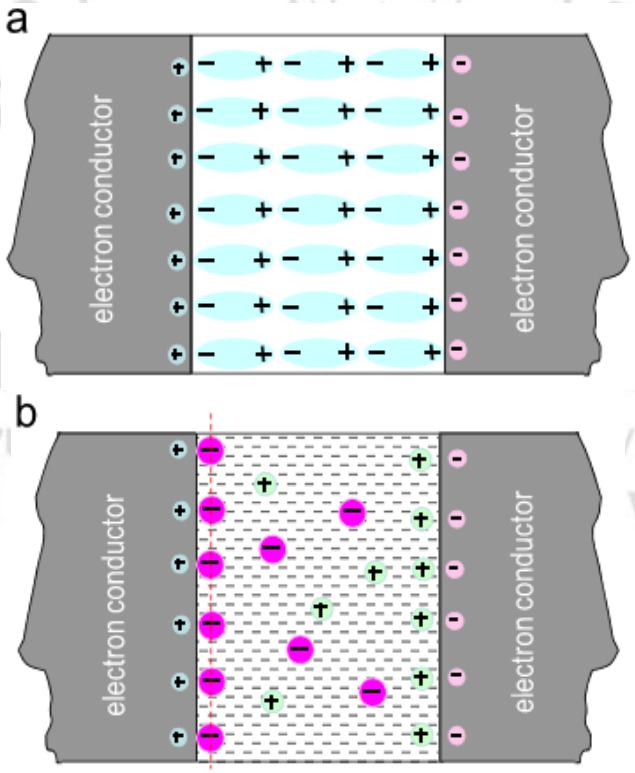

Figure 2.3 The construction of (a) conventional capacitors and (b) EDLCs capacitors [49].

To fit with the most important test of electrochemical properties e.g. cyclic voltammogram (CV). The equation 2.2 can be rearranged to

$$Q = CV \tag{2.3}$$

The test examines the current response to the variation of voltage with time (t) and assumes that C is constant. The differential of equation 2.3 can be expressed as

$$\frac{dQ}{dt} = C\frac{dV}{dt} = V\frac{dC}{dt} = C\frac{dV}{dt} \tag{2.4}$$

Assuming that the applied voltage varies linearly with time. Thus, $V_0 + \nu t$ here V_0 is the initial voltage (V), which may be equal to zero. Then $\frac{dV}{dt} = \nu$ is voltage scan rate (V/s). The potential scan rate (ν) is commonly known in the CV electrochemical test that it is related to the velocity, which is the rate of change of voltage as a function of time. For the current, $i = \frac{dQ}{dt}$, so the equation 2.4 can be rewritten as

$$C = i\nu \tag{2.5}$$

The equation 2.5 shows that the capacitance is proportional linear with the current (i) and scan rate (ν) but it is independent of voltage (V). It is marked that ν is positive or negative, depending on the increasing or decreasing voltage. Leading to the current can be also positive or negative value relates to the direction of the scan rate. Expressly, when the voltage scan is sweeply reversed in direction with a constant rate of scan, the current will skip from a positive value to a negative value, as seen in the CV pattern from the electrochemical test (Figure 2.4).

The pattern of equation 2.5 can be plotted to the rectangular i-V curve with the different scan rate as shown in Figure 2.4 [49]. The CV test generally uses for qualitative ifying the capacitive behavior of the electrochemical energy storage devices. In the galvanostatic charged-discharged (GCD) electrochemical test, it applies a constant i for charging/discharging (positive/negative current) the capacitor electrode and detects the changing of constant voltage. Hence, the schematic graph between voltage and time during the applying of a constant current, which is mean that the equation 2.5 is

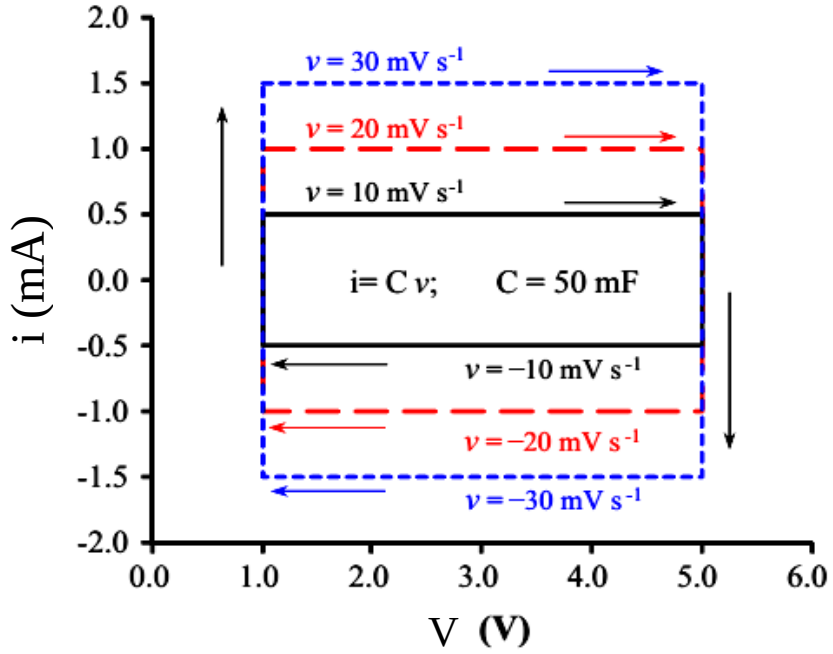

Figure 2.4 The rectangular i-V curve with the variation of the scan rates for C = 50 mF, V_{max}= 5 V [49].

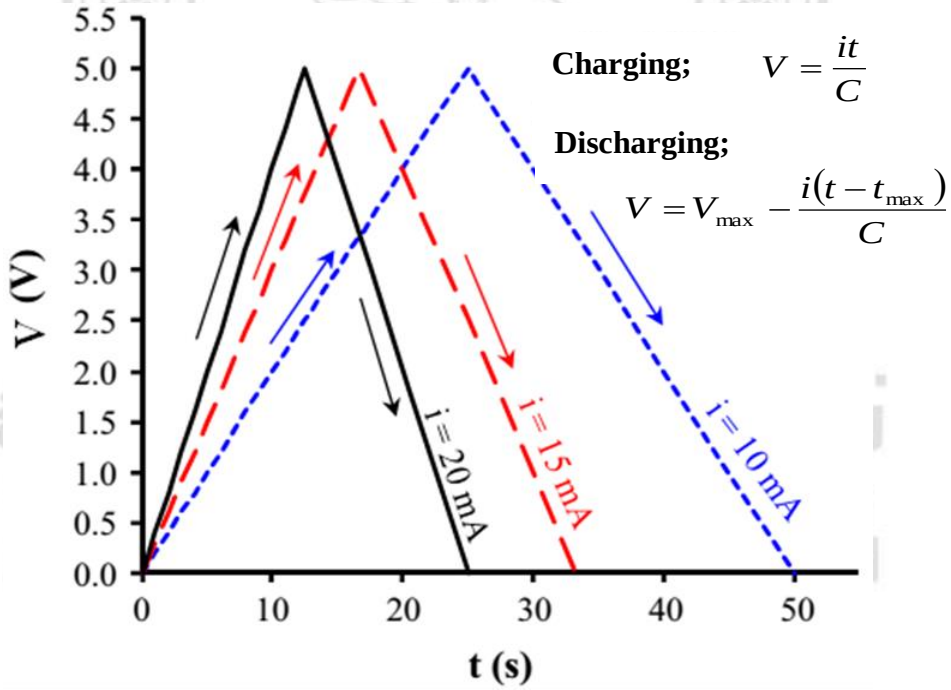

Figure 2.5 Schematic representation of GCD graph at constant currents as achieved from equation 2.5, for C= 50 mF, $t_{max} = \frac{V_{max} C}{i}$

integrated ($C = i\int_{V_0}^{V_{max}} V\frac{dV}{dt}$) can be illustrated in Figure 2.5. Practically, most active materials for using as the EDLCs capacitors electrode such as the carbonaceous materials, comprising graphenes, carbon nanotubes and activated carbons usually have the electrochemical performances, of which relate to the CV and GCD patterns as illustrated in Figure 2.4 and 2.5.

1.2) The pseudocapacitors

The other type of supercapacitors is the pseudocapacitors. The capacitance takes place for the reasons of thermodynamic (equation 2.2), which is the amount of charge storage (Q) and the change of voltage/potential (V) [48]. This capacitance refers to the pseudocapacitance. The pseudocapacitors have the main mechanism dissimilar the EDLCs capacitor. That is the charge storage base on fast redox reaction with faradaic charge transfer between ions in the electrolyte and partial electro-active species of electrodes. Transition metal oxide (TMOs) such as ruthenium oxide (RuO_2) [50, 51] and manganese oxide (MnO_2) [52], conductive polymers e.g. polyaniline (PANi) and polypyrrole [14] and etc. are the most well-known as the active materials for pseudo-capacitor applications. The good point of pseudocapacitors is its capacitance value higher than the EDLCs capacitors. However, the practical limitations are found. They not only have low power densities because of their intrinsic electronic conductivity (high resistivities) but also have unstable at a long-term cycling.

The higher capacitance more than the EDLCs capacitor are gained in the active materials of pseudocapacitors, some case higher up to nearly 100 times. This is attributed to their characteristic of the materials used, which usually employ the nanostructured TMOs. Thus the high surface area (good for the EDLC mechanism) and the advantage of the oxide (good for the redox activities) can be enhanced the electrochemical performance [53].

Figure 2.6 describes the mechanism of charge storage base on ion intercalation/depletion, which occurs inside the pseudo-capacitive materials [53]. When charging process happens, the electrons from the redox reaction will move so left the positive charges on the electrode surface for balancing ions. Resulting in the concentration gradient occurring during the process, which is the effect of the

anion diffuse from the electrolyte to the active material. In the discharging process, the inverse mechanism will happen [54]. The architecture of the active material is as significant as in EDLCs mechanism due to the main reaction begin at the interface between active material/electrolyte.

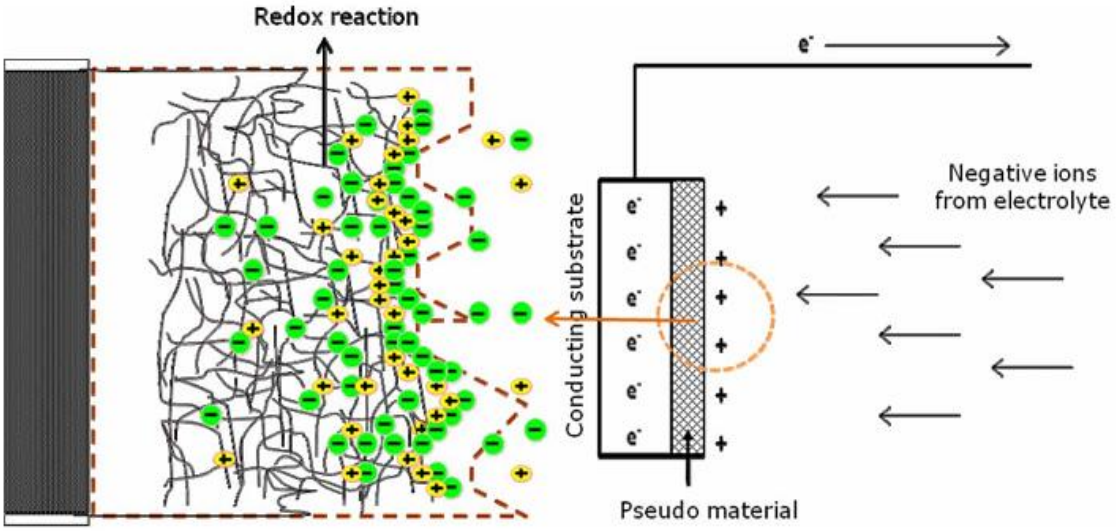

Figure 2.6 The charge storage procedure in a pseudo-capacitive material. The highlight is the intercalation of electrons (anions) for balancing of the positive charge, which comes from the oxidation process [53].

The ruthenium oxide is the excellent pseudocapacitors materials, it has a good conductivities and high reversibility several surface redox couples [48, 55]. The amorphous and crystalline phase of the ruthenium oxide has been broadly investigated with characterization under the acidic electrolyte solution. It is found that the ruthenium oxide with amorphous hydrous phase $RuO_2 \cdot xH_2O$ shows the capacitance much higher than the anhydrous crystalline phase [51]. This is because the mixed electronic-protonic conductor [56], which is the superficial redox activities, relating to the double injection/ejection of protons and electrons as shown in equation below [48, 57];

$$RuO_x(OH)_y + \delta H^+ + \delta e^- \Leftrightarrow RuO_{x-\delta}(OH)_{y+\delta} \quad (2.6)$$

Here $RuO_x(OH)_y$ and $RuO_{x-\delta}(OH)_{y+\delta}$ show the interfacial oxyruthenium species at the oxidation states of high and low. In the electrolyte which is H_2SO_4, the faradic charges can be stored/delivered via the redox transitions of the oxyruthenium groups,

reversing between Ru^{4+}/Ru^{3+} and Ru^{3+}/Ru^{2+}. Leading to the $RuO_2 \cdot xH_2O$ had very high theoretical specific capacitance approximately 1300-2200 F/g [50]. In 2004 Hu et al. first group investigated a pure bulk $RuO_2 \cdot xH_2O$ and achieved capacitance value is nearly 1300 F/g. As shown in equation 2.5, it is described that the good performance not only came from the proton exchange and electron-hopping process but also the surface of hydrous oxide, which helps to enhance the rate of redox transfer (a proton liquid) [58]. Although this material is promising for use as the electrodes in the energy storage application, it does not succeed to use in the commercials. Due to it very expensive.

Concerning the electrochemical properties of the pseudocapacitors, it should be noted that despite the pseudo-capacitor store energy base on the faradaic process, in CV and GCD test it should not deal with the redox peaks. That is the results from both of techniques should agree with the EDLCs capacitor, which is box-shaped like in CV and triangular in GCD [49] (Figure 2.4 and 2.5). Furthermore, it is important to note that not overall faradaic process are the characteristic of pseudocapacitors. The fuel cell and rechargeable batteries (non-capacitive) also have the faradaic in nature.

The faradaic reaction is also the main mechanism of the rechargeable batteries for storage charges. However, the typical CV and GCDs pattern are unlike the EDLCs capacitors and pseudocapacitors. The results evaluate the pattern of oxidation/reduction peaks on the CV pattern and plateau charged/discharged on the GCD graph. Because the performance of the battery electrodes sturdy depends on the redox reaction, resulting to they are operated within the narrow potential window. The typical CV and GCD pattern of the battery electrode are depicted in Figure 2.7 (a) and 2.7 (b) [49].

In Figure 2.7, it is assumed that the reverse of the faradaic process (redox peak) is shown as the symmetrical pattern, the CV and GCD symmetric result in the X-axis and Y-axis, respectively. Nevertheless, the fact that almost commercial batteries have very small reversible reactions on the electrodes. This is because they have diverse polarizations, attributing the ohmic resistance, the hard of ion transport and the kinetic barriers for electron transfer [49]. So, the CV result of positive electrode usually represents oxidation peak at higher than that of the reduction peak. Also, the GCD result shows the charging potential plateau more positive potential than the discharging. In Figure 2.7, it is assumed that the reverse of the faradaic process (redox peak) is shown

as the symmetrical pattern, the CV and GCD symmetric result in the X-axis and Y-axis, respectively. Nevertheless, the fact that almost commercial batteries have very small reversible reactions on the electrodes. This is because they have diverse polarizations, attributing the ohmic resistance, the hard of ion transport and the kinetic barriers for electron transfer [49]. So, the CV result of positive electrode usually represents oxidation peak at higher than that of the reduction peak. Also, the GCD result shows the charging potential plateau more positive potential than the discharging

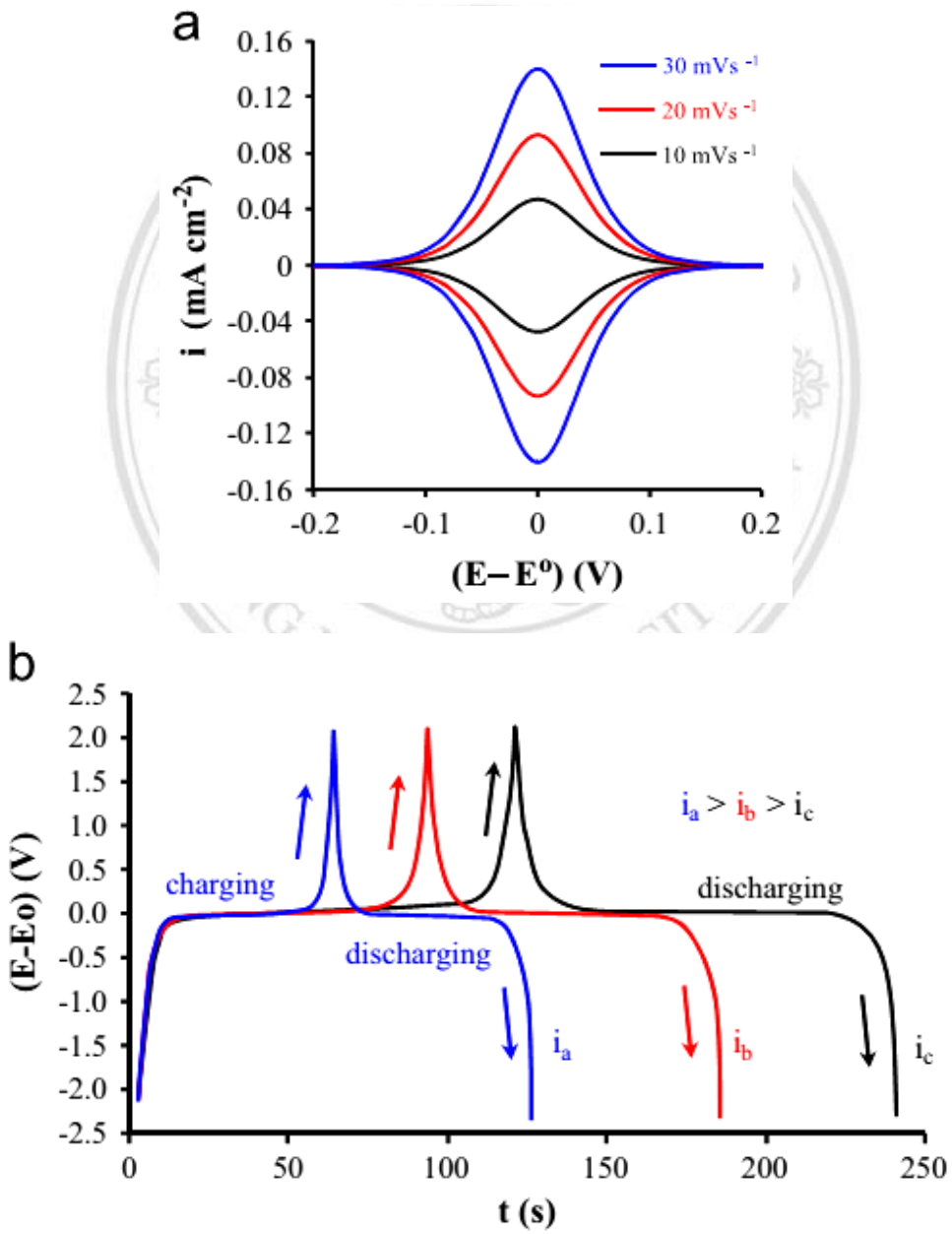

Figure 2.7 (a) CV pattern at a various scan rate and (b) GCD graph with a different charged/discharged current of an assumed positive battery electrode [49].

Recently, the band theory can be used to elucidate the charge storage of pseudocapacitors [52, 53] as depicted in Figure 2.8. It shows the distribution of electronic energy states consist of insulators, semiconductors, and metals. It is seen that the metal illustrates fully overlapped electron energy states that allow the free electron moving response to the electrical field [53]. Thus, in this case, it unable to storage charge and it can be found the straight-line CV pattern. In contrast, in the case of insulators, these materials have a wide band gap energy. So electron transfer process can be difficult to occur [59]. But, some insulative materials may have the redox active molecules or ions in an electrolyte solution, which can be transferred under an optimal condition or optimal potential. The CV result of these materials exhibit the redox peak with a narrow potential range [49] (Figure 2.7 (a)). It should be pointed out that this characteristic is non-capacitive materials. Due to the current from the redox reaction responds linearly with the potential deviation. Thus, it should be indicated to a battery-type behavior.

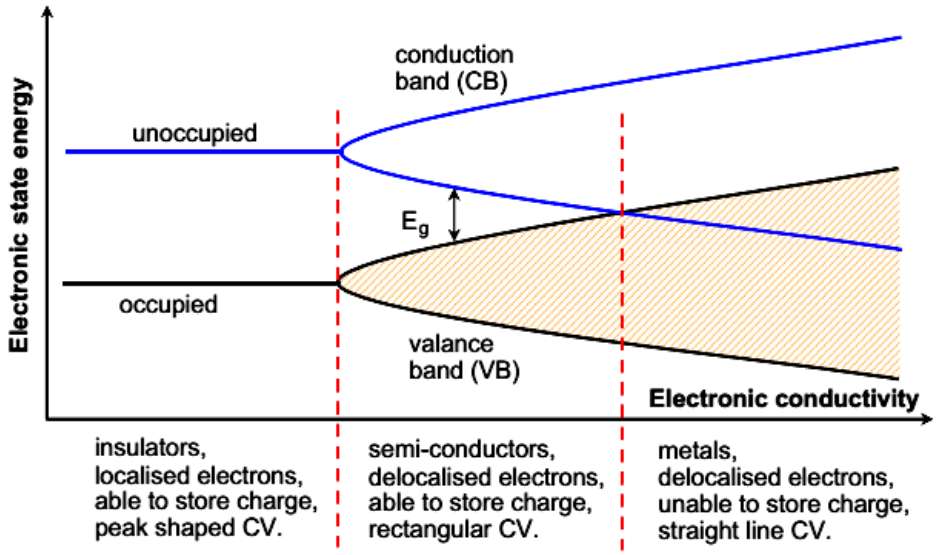

Figure 2.8 The band theory and its deal with conductivity, charge storage performance and pattern of insulators, semiconductors and metals [49].

For semiconductors, since the band gap energy of these materials are smaller than the insulative material, the active sites for redox activities are easy to react with one another [49]. Moreover, the semiconductors are good conductivity, resulting to the electron can be facilitated to transfer continuously. Thus, the energy state can combine into a wide-ranging band with small differences between the neighboring states [49]. This behavior makes the constant current flow with the variation of the potential in a

wide range [53]. Obviously, this nature of semiconductors (also fund conducting polymer) can be called the pseudo-capacitive characteristic. Also, these materials can be achieved the box-shaped CV pattern.

2) The capabilities of supercapacitors [49]

The storing energy process begins with when applied voltage/potential (V) through the devices with a short time (t). The small quantity of work is done to split or keep a small amount of charge (dQ) to collect at the interface between electrode and medium. Assuming an ideal capacitor, the overall work is equal to the total energy of the capacitor, which can be stored. Relating to the equation (2.2) the relation between dW and dQ can be showed as follow;

$$dE = dW = VdQ = \frac{Q}{C}dQ \tag{2.7}$$

By integration of the equation (2.7), the equation (2.8) can be expressed below;

$$E = W = \int_0^Q \frac{Q}{C}dQ = \frac{1}{2}\frac{Q^2}{C} = \frac{QV}{2} = \frac{CV^2}{2} \tag{2.8}$$

From equation (2.8), it is seen that the voltage is proportional to charge storage in the capacitor. Practically, the failure of the capacitor mainly comes from the breakdown of medium (dielectric) at the maximum voltage (V_{max}). So, the maximum energy (maximum capacitance) of the device is limited by the category of the medium used or the V_{max} [49].

The power (P) of the capacitor is the energy delivery performance, which is achieved by using the equation (2.9)

$$P = \frac{W}{t} = \frac{CV^2}{2t} \tag{2.9}$$

Here, t is discharged time, it is clearly seen that the maximum power (P_{max}) is obtained by having the shortest discharged time. It should be considered the internal resistance of the capacitor, which named as equivalent series resistance (ESR).

The simple RC circuit can be displayed in Figure 2.9.

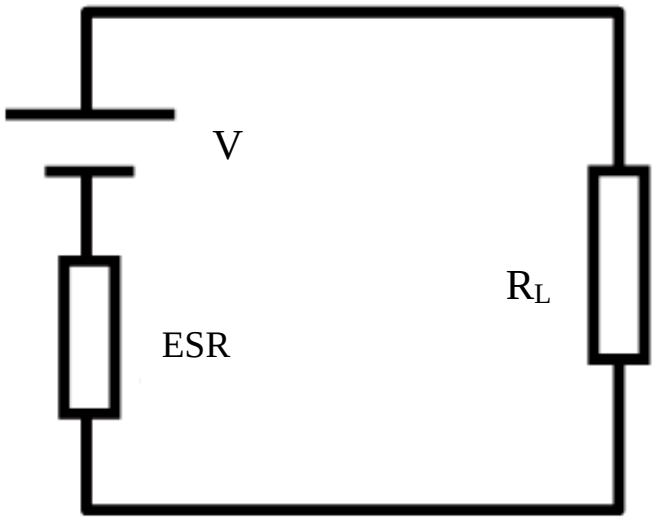

Figure 2.9 The schematic illustration of RC circuit [49].

Figure 2.9 consists of load (R_L), ESR. and power supply (V). Regarding the power supply deliver the current pass the circuit, the Ohmic law should be used to descript as shown in equation (2.10)

$$V = iR \tag{2.10}$$

From above the total resistance and the power passing the load can be achieved as equation (2.11) and (2.12).

$$R = R_L + ESR \tag{2.11}$$

$$P = iV = i^2 R_L \tag{2.12}$$

From equation (2.11) and (2.12), the power of the circuit can be obtained as follow;

$$P = \left(\frac{V}{R_L + ESR} \right)^2 R_L = \frac{V^2 R_L}{(R_L + ESR)^2} \tag{2.13}$$

It is found that from the equation (2.13) the maximum power can be achieved when R_L is equal to ESR. Thus, it can be rewritten the equation (2.13) as below;

$$P_{max} = \frac{V^2 ESR}{(ESR + ESR)^2} = \frac{V^2}{(4ESR)} \tag{2.14}$$

The equation 2.14 shows the P_{max} as a function of V and ESR. However, if want to consider the capacitance (C) relate to the ESR can be given the equation (2.14) to equation (2.9). Furthermore, to get the P_{max}, it should be assumed at t_{min} (as shown in equation 2.15)

$$t_{min} = \frac{CV^2}{2P_{max}} = \frac{CV^2}{2(\frac{V^2}{4ESR})} = 2CESR \tag{2.15}$$

Although enormous experimentations usually report the performance of the energy storage devices by using the equation (2.14). Interestingly the equation (2.15) is also very helpful and significant. It can be used to design the devices for optimizing the system. To illustrate if we desire to get a better system, which can deliver energy at long time operation (Wh/kg), the batteries and fuel cells are still superior choices than the supercapacitors.

2.1) The conductive current collector

The conductive current collector is the one important components of the energy storage devices, which should be considered. It can be adjusted for minimizing the internal resistance and optimizing the electrochemical performance of the devices. The optimal conductive current collector must has low resistance, stable under the high potential operation in various electrolytes and good contact with the active materials. To get the good properties, the different methods are used to modify. To illustrate, it is found that the surface polishment of Al current collector can be decreased the surface resistance between the Al and the active material. Furthermore, the heat treatment process can be used to enhance the stability of the devices at long-term cycles [60]. Due to the high surface area and good conductivity, the Ni foams are the better choice for employing as the conductive current collector than the metal sheets/foils. Other current collector materials can be found such as the Ni plaque [61] and the carbonaceous materials, consisting carbon aerogel [62], carbonized sponge [63] and the vertical grown CNT [64].

2.2) The separator

Generally, the separators are used to divide the two electrodes of the devices, avoiding the short circuit. It includes a lot of porous and tunnels for ion in electrolyte easy to transport pass through. The main key factors should be considered e.g. pore size, thickness, absorbency, permeability, puncture resistance, chemical stability, thermal properties and tensile strength. To illustrates, the internal resistance is proportional to the permeability of the separator. Because this value can be indicated that how facile the ions and molecule in electrolyte move pass it. Also, the separator thickness has the influence to the internal resistance and permeability. So, the thickness should be modified when fabricated the complete cell. The absorbency evaluates the ability to absorb the electrolyte. This value directly relates to the wet ability of the separator. Thus, the good absorbency should be decreased the internal resistance of the devices. In the point of chemical stability, it commonly knows that the separator with a superb chemical stability can enhance the cycling ability. Moreover, the separator should has the high tensile strength, good puncture resistance and high thermal properties, which strength enough for use with the roughness surface of the electrode. The commercial separators have been employ in energy storage application are shown in Table 2.1

Table 2.1 Some properties of some commercial microporous membranes separators [65].

Properties/ Separators	**Celgard 2730**	**Celgard 2400**	**Celgard 2320**	**Celgard 2325**	**Asahi Hipore**	**Tonen Setela**
Structure	Single layer	Single layer	trilayer	trilayer	Single layer	Single layer
Composition	PE	PP	PP/PE/PP	PP/PE/PP	PP	PP
Thickness (um)	20	25	20	25	25	25
gurley (s)	22	24	20	23	21	26
Ionic resistivity[a] (Ω cm^2)	2.23	2.55	1.36	1.85	2.66	2.56
Porosity (%)	43	40	42	42	40	41
Melt temp (C^o)	135	165	135/165	135/165	138	137

[a]In 1M $LiPF_6$ Ethylene carbonate:ethyl methyl carbonate (30:70 by volume)

2.3) Electrolyte

Electrolyte, which generally uses in electrochemical energy storage can be classified into aqueous, organic, and ionic liquids. Two important factors; for example, electrochemical stability and ionic conductivity should be regarded for selection of the electrolyte. The window potential/voltage window directly depend on the electrolyte and also has an effect to the energy density and power density of the devices. The aqueous electrolyte such as alkali group (i.e. NaOH, KOH), acidic group (i.e. HCl, H_2SO_4) and neutral solution group (Na_2SO_4, Li_2SO_4). These electrolytes have high ionic conductivity nearly up to ~1 S cm^{-1}. So, the high power density can be obtained. However, the electrolysis of water (standard potential) are found at ~1.23 V. Therefore, the devices using aqueous electrolyte usually have a narrow voltage window (≤ 1.0 V) and have a low energy density [66]. The voltage window can be increased up to ~3.0 V when using the organic electrolyte but it is found that the ionic conductivity and the specific capacitance are low as illustrated in Table 2.2.

Table 2.2. The specific capacitance relates to the electrolytes materials [67]

Materials	**Density ($g\ cm^{-3}$)**	**Electrolytes**	**Specific Capacitance ($F\ g^{-1}$)**
Carbon cloth	0.35	KOH	200
		Organic	100
Carbon black	1.0	KOH	95
Aerogel carbon	0.6	KOH	140
Particulate from SiC	0.7	KOH	175
		Organic	100
Particulate from TiC	0.5	KOH	220
		Organic	120
Anhydrous RuO2	2.7	H_2SO_4	150
Hydrous RuO2	2.0	H_2SO_4	650
Doped conducting polymers	0.7	Organic	450

It is found that the organic electrolytes have selected to use in the commercial industries for high energy density application. Commonly, they use the propylene

carbonate and acetonitrile as the organic electrolytes and the tetraethylammonium tetrafluoroborate is employed as a salt, which is dissolved in a solvent. The ionic conductivity can be adjusted by the adding of the salt until reach to the maximum dissolved [68].

Ionic liquids have been considered as the promising electrolytes for electrochemical energy storage devices. They are molten salts at room temperature. Their advantages consist of low vapor pressure, large voltage window, and good thermal property [69-72]. However, they have the limitation in ionic conductivity at room temperature, leading to the decreasing of the power performance [73]. The CV difference of voltage window between H_2SO_4 aqueous electrolyte and $TEABF_4$ (tetraethyl ammonium tetrafluoroborate) in acetonitrile organic electrolyte is evaluated in Figure 2.10.

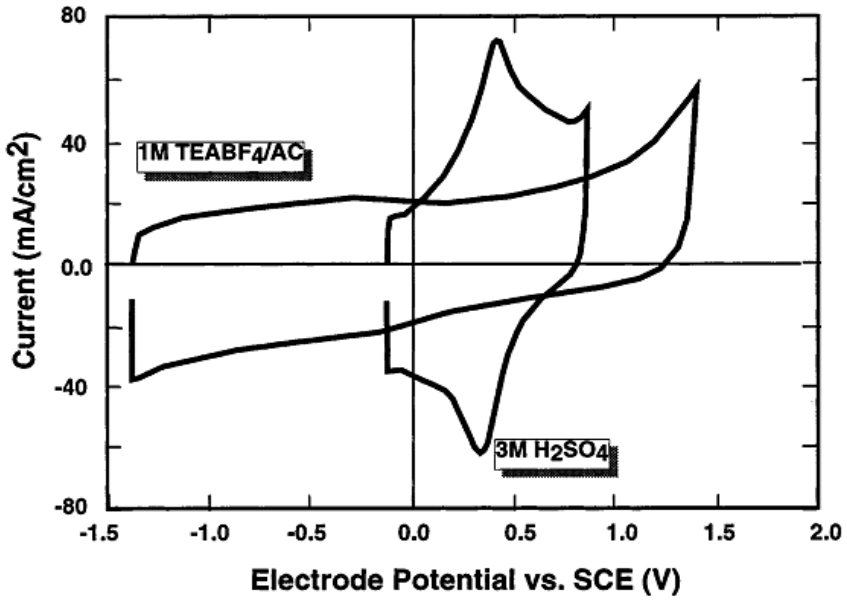

Figure 2.10 CV pattern of activated glassy carbon electrodes in 3 M H_2SO_4 aqueous electrolyte and in 1 M TEABF4 in acetonitrile at the scan rate of 100 mV/s [46].

2.4) Ragone plot

Ragon plot in Figure 2.11 represents the relation of energy densities vs. power densities with a log scale. This plot generally uses to compare the performance of wide-ranging of energy storage devices]. The energy density and power density descript about how it quickly charged/discharged (W/kg) and how much energy is available (Wh/kg), respectively.

Moreover, in Figure 2.11 it is seen that the capacitors locate on the top left side of the graph while the batteries and the fuel cells place on the bottom right side, implying that the capacitors have high power density and low energy density. In contrast, the batteries and the fuel cells have low power density and high energy density. This characteristic is inferred that the capacitors have a faster rate charging/discharging or deliver the energy with shorter time but they have lower capabilities of energy than the batteries and the fuel cells. The supercapacitors situate on the center of the Ragone plot between the capacitors and the batteries as well as the fuel cells. It can be said that the performance of supercapacitors is intermediate between the high energy density and high power density. Thus, they can be fulfilled some limitation properties of both devices, which previously mention. With remarkable advantages of supercapacitors, they have recently much received considerable attention and have been widely used in potential applications i.e. the fields of the power system, the vehicle assistant equipment, power sources for emergency doors on jet planes and the memory storage [74].

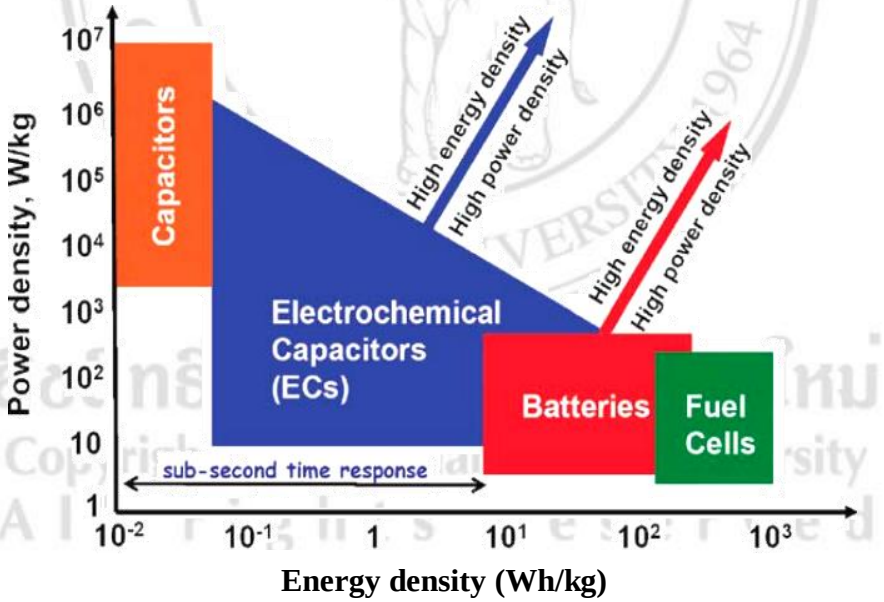

Figure 2.11 Ragone plot presenting energy density against power density of the various energy storage devices [75].

Moreover, in Figure 2.11 it is seen that the capacitors locate on the top left side of the graph while the batteries and the fuel cells place on the bottom right side, implying that the capacitors have high power density and low energy density. In contrast, the batteries and the fuel cells have low power density and high energy density. This

characteristic is inferred that the capacitors have a faster rate charging/discharging or deliver the energy with shorter time but they have lower capabilities of energy than the batteries and the fuel cells. The supercapacitors situate on the center of the Ragone plot between the capacitors and the batteries as well as the fuel cells. It can be said that the performance of supercapacitors is intermediate between the high energy density and high power density. Thus, they can be fulfilled some limitation properties of both devices, which previously mention. With remarkable advantages of supercapacitors, they have recently much received considerable attention and have been widely used in potential applications i.e. the fields of the power system, the vehicle assistant equipment, power sources for emergency doors on jet planes and the memory storage [74].

3) Electrode materials for use as supercapacitors

Various materials, which can be employed to use as the electrode of supercapacitors can be classified into 3 main categories, depending on the charge storage mechanism, as depicted in Figure 2.12. Focusing on the electrode materials used (Figure 2.12), it is seen that the EDLCs capacitors group contain the various kind of carbon materials electrodes such as activated carbon, carbon nanotube carbon aerogels and graphene. The pseudocapacitors consist of the conductive polymer and TMOs. Last is hybrid capacitors. This type storing charge relies on the combination of EDLCs and pseudocapacitor mechanism, which can be divided to the composite, asymmetric and battery-type hybrid. Many literature surveys about these materials can be discussed as follow;

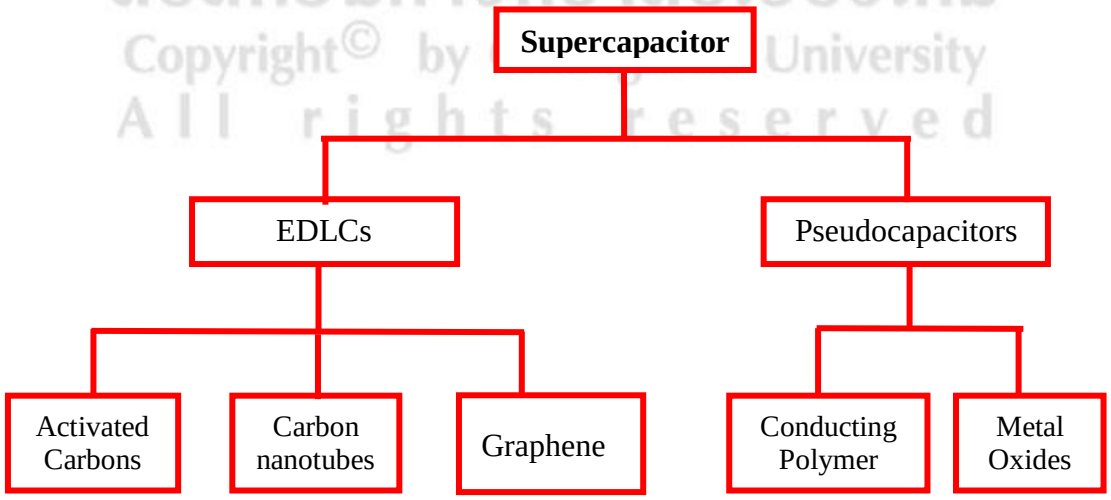

Figure 2.12 The group of supercapacitors and its electrode materials used.

3.1) Carbon materials for supercapacitor electrode

3.1.1) Activated carbon (AC)

With high surface area and mesoporous feature, leading to the activated carbon have been generally using as the electrode of EDLCs capacitor type [76-78]. It is found that the specific surface area of the AC is approximately 1000-2000 $m^2\ g^{-1}$. In fact, the AC with 1000 $m^2\ g^{-1}$ should has the capacitance value in the range of 200-500 F g^{-1} [76]. Unfortunately, in practical application, the obtained capacitance is only ~10 F g^{-1}. This is attributed to the main other factors, which has direct effect on the EDLC mechanism. That is its pore size of the AC, consisting a wide ranging pore size distribution e.g. macroporous (> 50 nm), mesoporous (2-5 nm) as well as micropores (< 2 nm) [77, 78]. Regarding the size of ion in the electrolyte solution, it is believed that the bigger ion size, such a case of the organic electrolyte cannot access through the smaller pore (microporous).

Commonly known as the specific capacitance has a strong association with a specific surface area of electrode materials. Nevertheless, not overall surface area can enhance the electrochemical performance because only the surface area contacts with the electrolyte (good wettability) can contribute the specific capacitance. So, it is found that the specific capacitance has a non-linearly relation with the specific surface area [79-81].

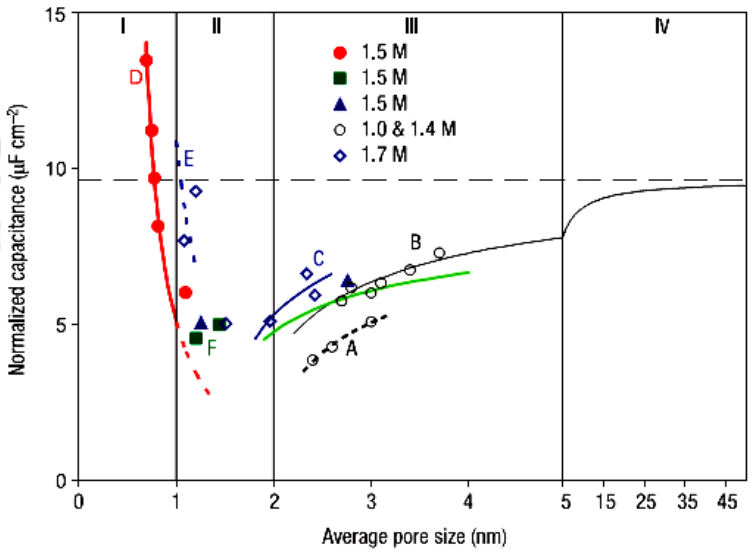

Figure 2.13 The specific capacitance normalized by specific surface area vs. average pore size of various carbon samples. A, B: templated mesoporous carbons; C: activated mesoporous carbon; D, F: microporous CDC; E: microporous activated carbon [82, 83]

Though the samples with smaller pore size should have high specific surface area, it is found that the solvated ions could not access the pores. Due to the pore with diameter < 0.5-1.0 nm for some bigger hydrated ions and solvated ions in organic electrolyte [80, 81, 84]. The pore size in the range of 2-5 nm has two times bigger than a solvated ion. The capacitance beginning increasing relate to pore size moderately [85, 86]. Nevertheless, the experimentation illustrates that the superb capacitive performance was achieved when used the particles with the balancing of micropore and mesopore. It is proved that the desolvated ions could path through the micropores and thus contributed to the specific capacitance of the materials [87]. As seen in Figure 2.13 the results showed that the normalized capacitance was gradually decreasing with average pore size until reach the critical value of about 1.5 nm, after that the normalized capacitance increased sharply with the decreasing of the average pore size to the ion size. Varying models are used for the different zones [40].

Recently the activated carbons have a high surface area but they have a low mesoporous that limited the electrochemical performance. Because of a low electrolyte accessibility and poor electrical conductivity, leading to a high internal resistance. So low power density (limited ~1-2 kW kg^{-1}) and low energy density (limited ~4-5 Wh kg^{-1}) have been achieved when using the AC as the electrodes [88]. New materials are required to solve this hindrance of this electrodes.

3.1.2) Carbon nanotubes (CNTs)

The CNTs have a high specific surface area [30,31], high aspect ratio and high electrical properties [89, 90]. They have been generally used as the active materials in supercapacitors [91-96]. The electrochemical performance of CNTs electrodes were found higher than the AC electrodes; for example, the free standing multi-walled carbon nanotubes (MWCNTs) had the specific capacitance of 102 F g^{-1}, energy density approximately 1 Wh kg^{-1} and power density up to 8 kW kg^{-1} in the H_2SO_4 solution [90]. Furthermore, the higher performances (180 F g^{-1}, the maximum power density and energy density ~20 kW kg^{-1} and 10 Wh kg^{-1} 1 mol L^{-1} in KOH electrolyte) had been obtained by employing the single-walled carbon nanotubes (SWCNTs) with the random orientation electrode [92]. The SEM of random distribution SWCNTs is shown in Figure 2.14. Although the research could achieve the better performance than the previous mention materials, the higher energy density still needs

to further increase. It is found that the agglomeration of SWCNTs and MWCNTs into the bundled structure or randomly entangle could reduce the specific surface area and thus diminish the specific capacitance [93] [97, 98].

The vertically aligned CNTs (VA-CNTs) have shown to be beneficial properties for supercapacitor applications. The SEM of VA-CNTs is depicted in Figure 2.15. They not only had the high tube-spacing but also good contacted to the conductive substrate (Figure 2.16 (a)), which facilitates for the ions adsorption/desorption on the electrode surfaces and could reduce the internal resistance. Hence, the materials can boost the electrochemical performances, consisting fast charging/discharging method and high long-term stable cycling performance.

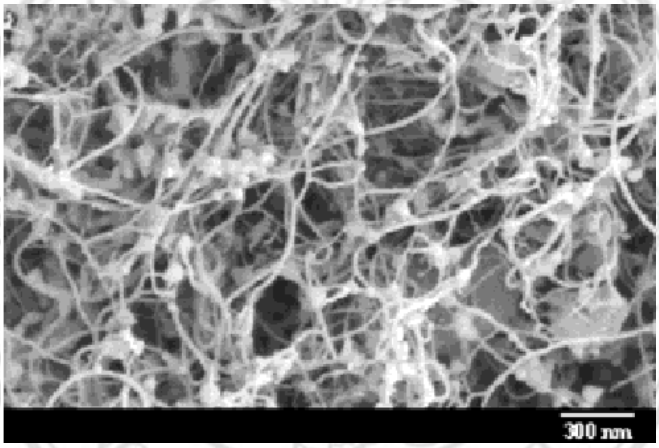

Figure 2.14 The SEM of random distribution SWCNTs [92]

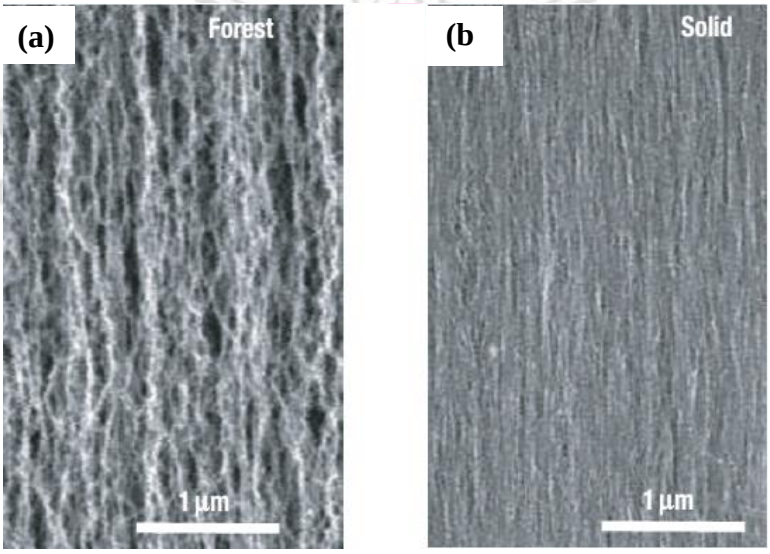

Figure 2.15 The SEM pictures of (a) the as-grown forest SWCNT (b) SECNT after liquid-induced densification process [93].

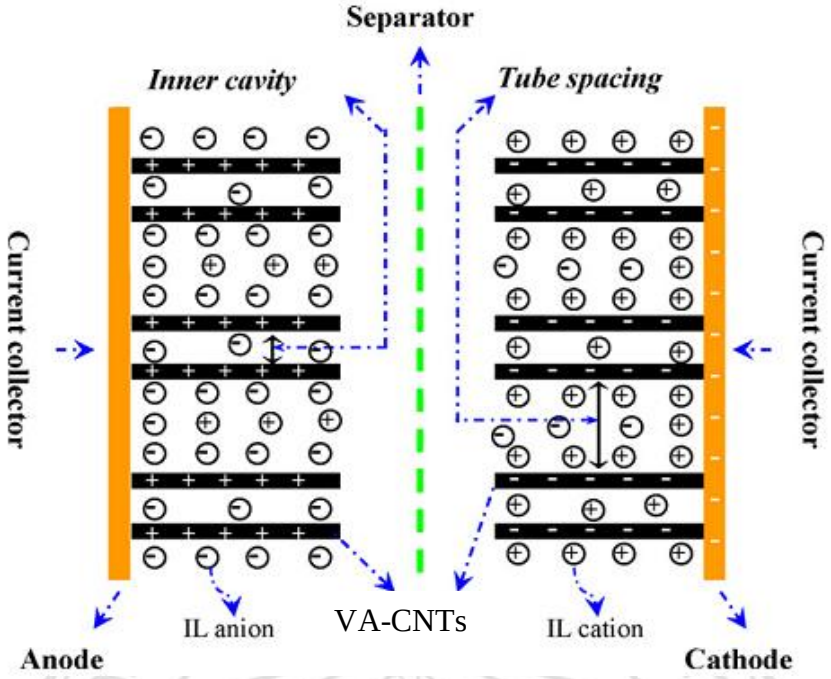

Figure 2.16 A schematic showing of the plasma-etched VA-CNTs used as supercapacitor electrode in an ionic liquid electrolyte (IL) [97].

Figure 2.16 demonstrated the schematic diagram of the plasma-etched VA-CNTs electrode. It is seen that the VA-CNTs were contacted directly onto a conductive current collector, raising the charge transport capability of the electrode. It is believed that the energy density could be enhanced because of the combination of all individual VA-CNTs. Moreover, the charges could be transported quickly through each VA-CNTs and thus the high power density could be achieved.

In addition, the VA-CNT arrays could be further optimized through the plasma etching process [97, 99]. The opened top end-caps of the samples were attained. These materials had the excellent electrochemical performance because the electrolyte could pass through the inner tube of the samples for charging storage. The morphology of the plasma-etched VA-CNTs is presented in Figure 2.17.

Many results showed that the VA-CNTs had the rate capability higher than the randomly align CNTs [93, 97-101], which had the energy density of 148 Wh kg^{-1} and power density of 315 kW kg^{-1} [102-105]. A high specific capacitance (365 F g^{-1}) was obtained when used VA-CNTs array electrode in 1 M H_2SO_4, synthesized by using a template-assisted CVD [103] and specific capacitance of 440 F g^{-1} was attained

From VA-CNTs prepared via a template-free CVD method in the ionic liquid electrolytes [106].

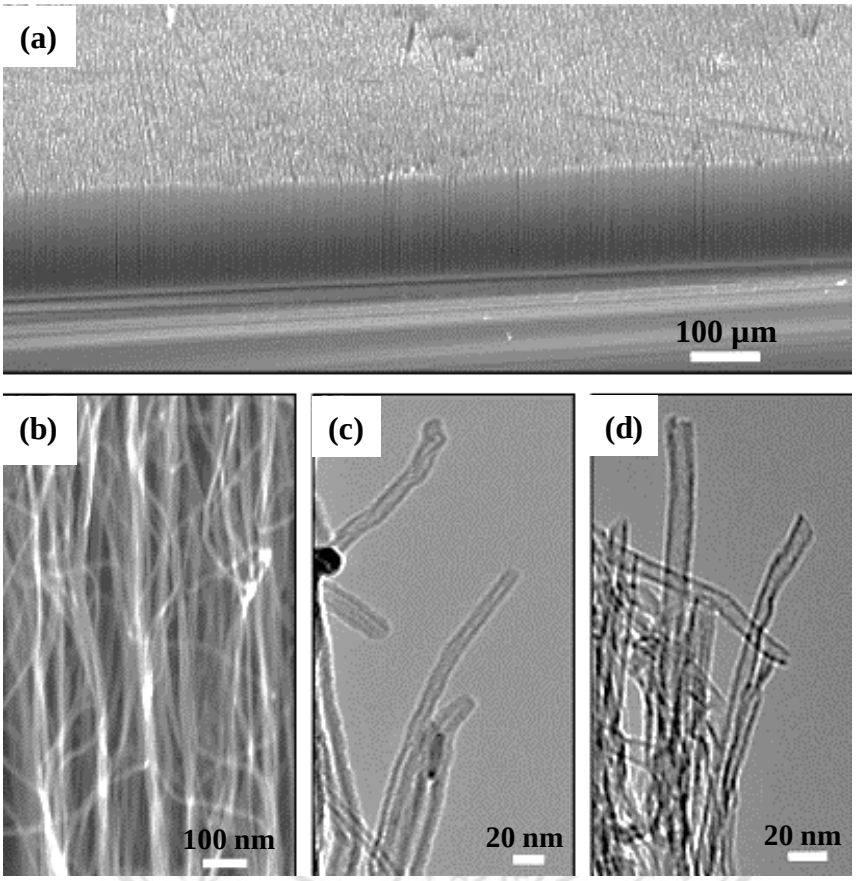

Figure 2.17 (a-b) low and high magnification SEM images of the plasma-etched VA-CNTs (c-d) TEM images of the sample before and after plasma etching [97]

Many results showed that the VA-CNTs had the rate capability higher than the randomly align CNTs [93, 97-101], which had the energy density of 148 Wh kg^{-1} and power density of 315 kW kg^{-1} [102-105]. A high specific capacitance (365 F g^{-1}) was obtained when used VA-CNTs array electrode in 1 M H_2SO_4, synthesized by using a template-assisted CVD [103] and specific capacitance of 440 F g^{-1} was attained from VA-CNTs prepared via a template-free CVD method in the ionic liquid electrolytes [106].

3.1.3)Graphene

Recently, graphene has attracted great interest in supercapacitor application owing to its high surface area, excellent carrier transport mobility and high thermal/mechanical stability [107]. The theoretical specific

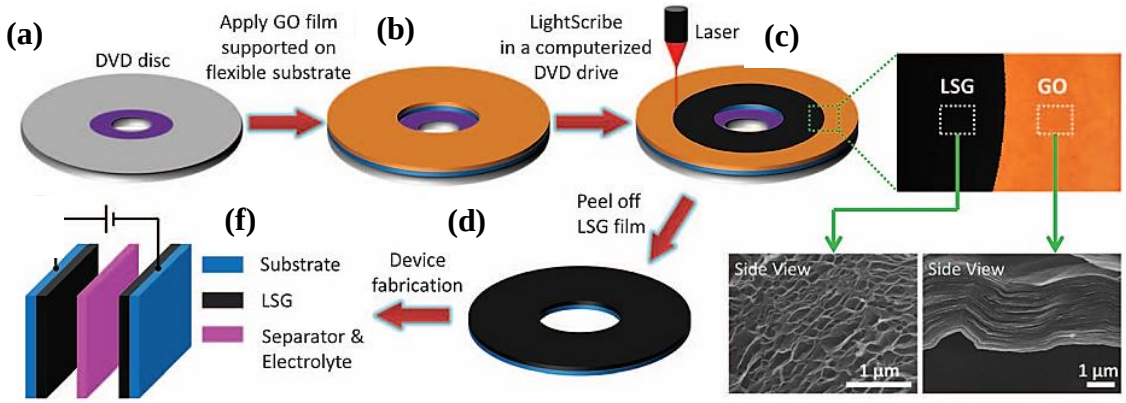

Figure 2.18 The Schematic diagram of the method of laser-scribed graphene (LSG) based on supercapacitor. (a-d) showed A step of reducing the GO film (golden brown color) to graphene (black color) via the LightScribe in a computerized DVD drive. (f) A symmetric supercapacitor is created, consisting two LSG electrodes, the separator and the electrolyte [108].

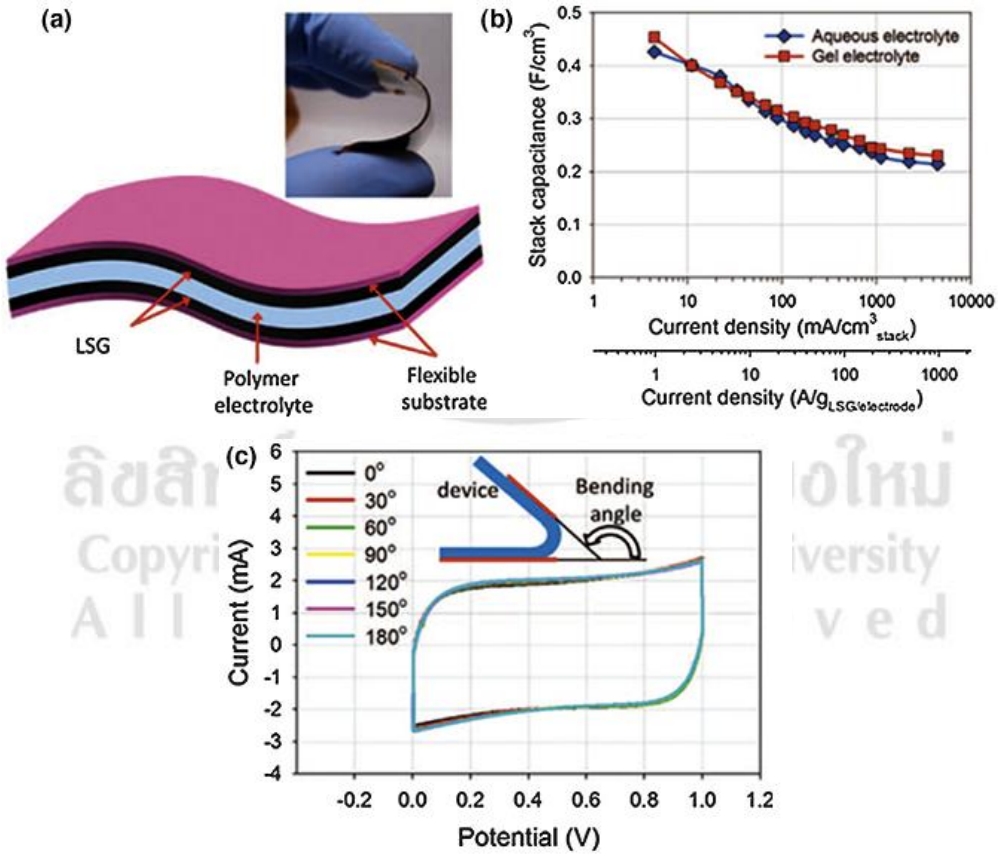

Figure 2.19 (a) Schematic diagram of the flexible supercapacitor based on LSG. (b) The performance of LSG-EC between a gelled electrolyte vs. an aqueous electrolyte. (c) The CV shape of the Flexible LSG-EC@ 1000 mV s^{-1} [108].

stability [107]. The theoretical specific capacitance of graphene electrodes are ~550 F g^{-1} which are the highest value among all carbon material electrodes [109, 110]. Base on chemically reduced graphene oxide (GO) electrodes. They had the specific capacitances of 135 and 99 F g $^{-1}$ in aqueous and organic electrolytes, respectively [111]. The high specific energy density has found ~85.6 Wh k g^{-1} and 136 Wh k g^{-1} at room temperature and at the temperature of 80 ºC [110].

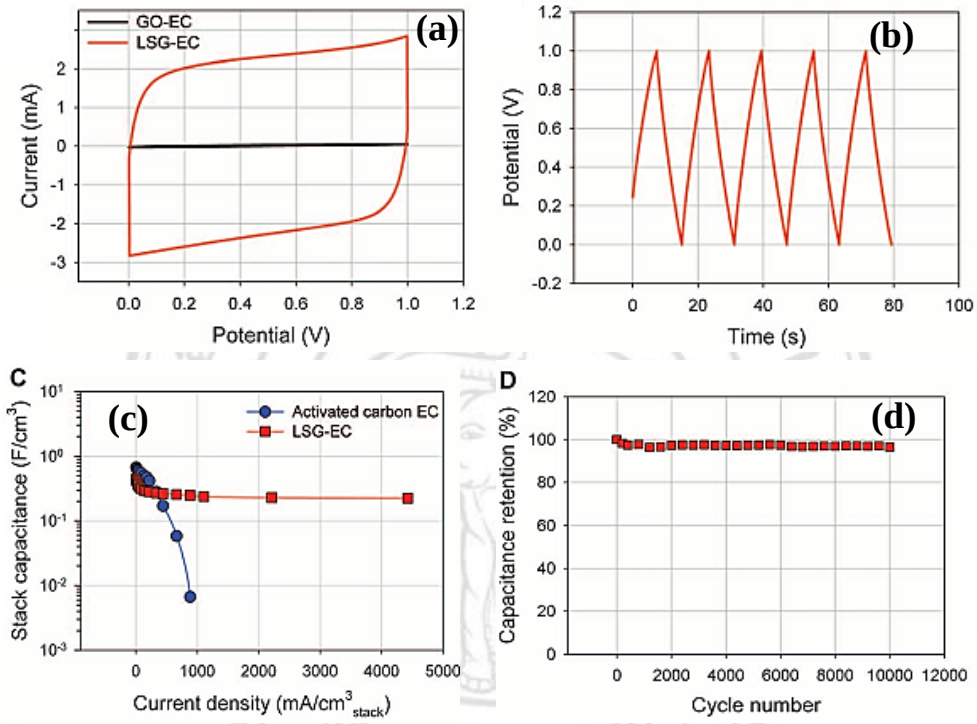

Figure 2.20 The performance of an LSG supercapacitors in 1.0 M H_3PO_4 electrolyte. (A) CV pattern of LSG and GO electrode @a scan rate of 1000 mV s^{-1}. (B) GCD characteristic of the LSG-EC @ 10 A g^{-1} LSG/electrode. (C) The volumetric stack capacitance of the LSG-EC is obtained from the GCD curves at different various current densities. The commercial AC supercapacitor (AC-EC) was used for comparison [108].

Lately, supercapacitors can be optimized by employing a LightScribe DVD optical for converting the GO films to graphene electrodes. They showed the excellent specific capacitance of 276 F g^{-1}, power density of 20 W cm^{-3} and the energy density of 1.36 mWh cm^{-3}, which 20 times and 2 times higher than the AC electrode, respectively. Also, the flexible electrodes evaluated exceptional stability when bending from 0º to 180º (Figure 2.19-2.20). The Schematic diagram of the method of laser-scribed graphene (LSG) based on supercapacitor are shown in Figure 2.18. The performance of GO

supercapacitor (GO-EC) and LSG supercapacitors (LSG-EC) showed a box-liked CV shape is observed for the LSG-EC, representing a double layer capacitor behavior (Figure 2.20).

3.1.4) Metal oxide for pseudocapacitors electorde

Ruthenium Oxide (RuO_2)

The ruthenium oxide is the excellent pseudocapacitors materials, it has a good conductivities and high reversibility several surface redox couples [48, 55]. The amorphous and crystalline phase of the ruthenium oxide has been broadly investigated with characterization under the acidic electrolyte solution. It is found that the ruthenium oxide with amorphous hydrous phase $RuO_2 \cdot xH_2O$ shows the capacitance much higher than the anhydrous crystalline phase [51]. This is because the mixed electronic-protonic conductor [56], which is the superficial redox activities, relating to the double injection/ejection of protons and electrons as shown in equation 2.14 [48, 57];

$$RuO_x(OH)_y + \delta H^+ + \delta e^- \Leftrightarrow RuO_{x-\delta}(OH)_{y+\delta} \qquad (2.14)$$

Here $RuO_x(OH)_y$ and $RuO_{x-\delta}(OH)_{y+\delta}$ show the interfacial oxyruthenium species at the oxidation states of high and low. In the electrolyte which is H_2SO_4, the faradic charges can be stored/delivered via the redox transitions of the oxyruthenium groups, reversing between Ru^{4+}/Ru^{3+} and Ru^{3+}/Ru^{2+}. Leading to the $RuO_2 \cdot xH_2O$ had very high theoretical specific capacitance approximately 1300-2200 F/g [50]. In 2004 Hu et al. first group investigated a pure bulk $RuO_2 \cdot xH_2O$ and achieved capacitance value is nearly 1300 F/g. As shown in equation 2.5, it is described that the good performance not only came from the proton exchange and electron-hopping process but also the surface of hydrous oxide, which helps to enhance the rate of redox transfer (a proton liquid) [58]. Although this material is promising for use as the electrodes in the energy storage application, it does not succeed to use in the commercials. Due to it very expensive.

Manganese dioxide (MnO_2)

MnO_2 has been used as a promising alternative to RuO_2 materials due to its cheap and excellent electrochemical performance [112-115] [19,20,35,36]. It is generally found that the performance of the materials are performed

in neutral electrolyte (Na_2SO_4, K_2SO_4) and mild acidic. In the acidic during testing, the partial of MnO_2 can be dissolve, which can be defined in equation (2.15) and (2.16) [116],

$$MnO_2 + H^+ + e^- \longleftrightarrow MnOOH \tag{2.15}$$

$$MnOOH + 3H^+ + e^- \longleftrightarrow Mn^{2+} + 2H_2O \tag{2.16}$$

In the neutral solution, it has two mechanisms, which is shown in equation (2.17) and (2.18) [117, 118].

$$MnO_2 + C^+ + e^- \longleftrightarrow MnOOC \tag{2.17}$$

$$(MnO_2)_{Surface} + C^+ + e^- \longleftrightarrow (MnOOC)_{Surface} \tag{2.18}$$

The equation 2.17 explains that the electrolyte cation (C^+) such as, Li^+, Na^+ and K^+ inserts into the electrode [117, 118]. The equation (2.18) shows the electrolyte cations adsorb on the surface of the MnO_2 electrode. These mechanisms relate to the redox reaction between the Mn^{3+} and Mn^{4+}.

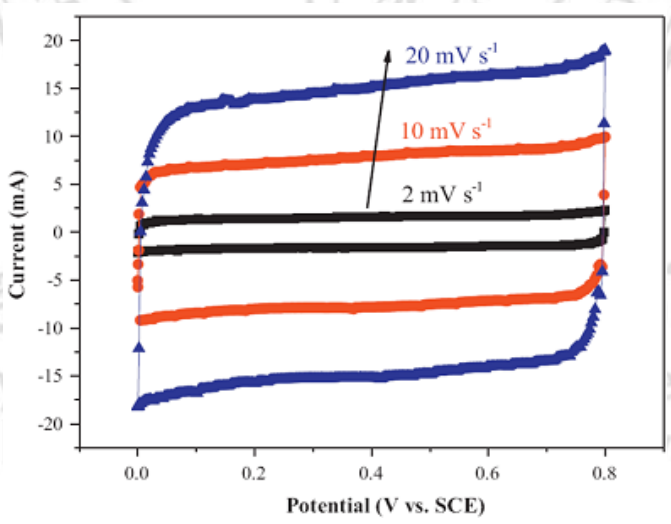

Figure 2.21 The CV pattern of MnO_2 at scan rate of 2,10,20 mV s^{-1} [4].

In Figure 2.21 show the rectangular CV pattern, which is described the fast reversible pseudocapacitive behaviors of MnO_2 electrode. The theoretical specific capacitance of MnO_2 is near about 1100 F·g^{-1} with potential window of 1.0 V. The theoretical specific capacitance can be calculated by equation (2.2)

$$C = \frac{Q}{V} = \frac{96485\ /(M_w)}{V} \tag{2.19}$$

Where 96485 C = the required amount of power use for electrolysis of 1 mol electrode materials is 1 F, M_W = molar mass, V= potential window (V).

However, in many research results, the specific capacitances of MnO_2 materials were found only five or ten times, which are lower than theoretical capacitance [119-123]. This is because of its low electronic conductivity (10^{-7} to 10^{-3} S cm^{-1}) [124]. The difference specific capacitance of MnO_2 depends on the crystallographic structures e.g. α, β, γ, δ, λ phase and their morphologies. For instance, the 2D tunnel structure of birnessite δ MnO_2 doped with potassium had a relatively high specific capacitance of 110 F g^{-1} [125]. The intermediate specific capacitance was achieved when using the 3D tunnel structure of λ-MnO_2 and relatively low specific capacitance was obtained with the 1D tunnel structure of γ- MnO_2.

3.1.5) Metal oxide for batteries-type electrode

Nickel oxide ((NiO)

NiO has a green and a cubic rock-salt crystal structure as shown in Figure 2.22. There is six coordination number both of nickel and oxygen atoms [2]. The NiO has excellent properties such as electrochemical properties, gas sensing and catalytic properties. It is widely employed in many fields, including electrochromic, catalysis and electrochemical energy storage application.

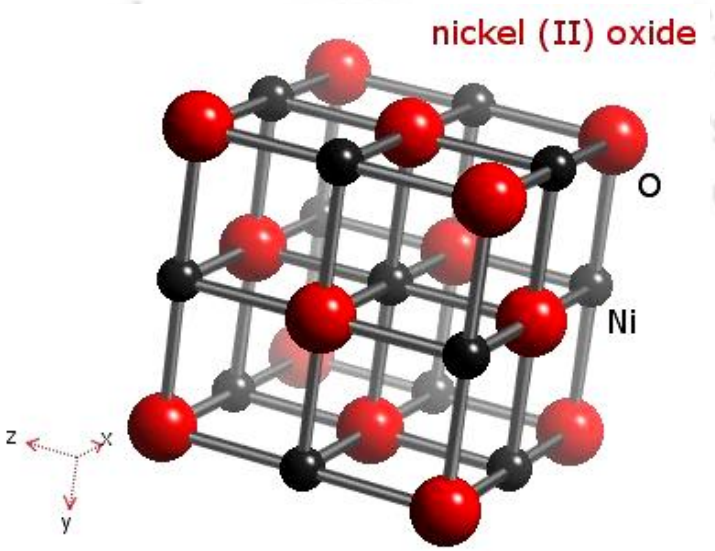

Figure 2.22 The cubic NiO structure [126].

NiO is a promising material for electrochemical energy storage devices, because of its high theoretical specific capacitance of 3750 F g^{-1}, environmental friendliness and cheap [127-129]. Two main mechanisms of NiO are considered that the charge are stored pass through the redox activity between NiO and NiOOH as depicted below;

$$NiO + OH^- \longleftrightarrow NiOOH + e^- \quad (2.19)$$

$$NiO + H_2O \longleftrightarrow NiOOH + H^+ + e^- \quad (2.20)$$

The first theory the redox reaction occurs via the Ni^{2+} oxidizes to Ni^{3+} (NiO to NiOOH) by the losing of an electron. Most studies tend to expand by using this theory, however, the second one should be considered as well. By the reason of the NiO can interact with OH^- in the alkaline solution, so it can produce the $Ni(OH)_2$, which will enhance the capacitance. The electrochemical reactions between $Ni(OH)_2$ and NiOOH are expressed in equation (2.21) and (2.22) [130-136];

$$Ni(OH)_2 \longleftrightarrow NiOOH + H^+ + e^- \quad (2.21)$$

$$Ni(OH)_2 + OH^- \longleftrightarrow NiOOH + H_2O + e^- \quad (2.22)$$

The NiO materials can be increased specific surface area for getting a better electrochemical performance such as short diffusion and transport pathways of ions and electrons, leading to fast redox reaction [132, 136]. Recently, most of the studies are focused on the synthesis approach and morphology of the NiO. Various techniques are used to fabricate NiO with a mesoporous and nanostructures for example:

-Sol-Gel Method: Three different morphologies of NiO nanostructures were prepared by a sol-gel method, including nanoflower-, slice- and particle-shaped NiO. The result showed that the NiO nanoflower with a three-dimensional network exhibited the best electrochemical performances [2]. Another shape of NiO had a lower specific capacitance because it's poor conductivity, resulting in a low electron transport. The SEM images of three different shaped NiO and the relative CV graph are shown in Figure 2.23.

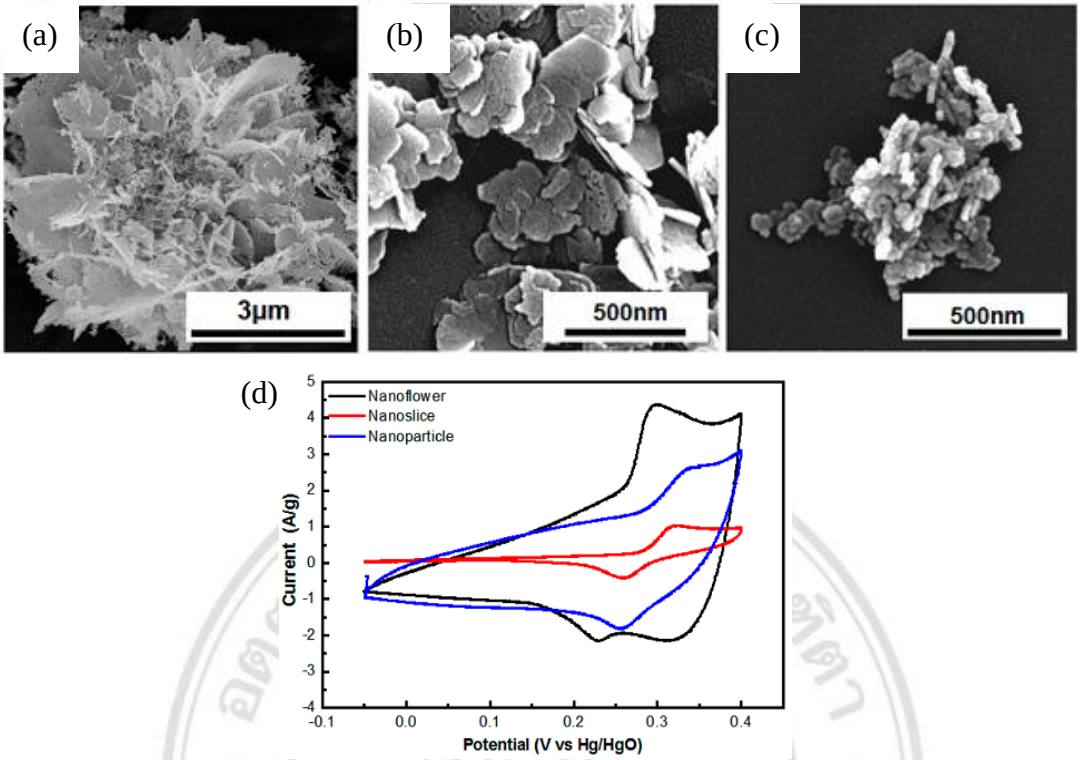

Figure 2.23 The SEM images of (a) NiO nanoflower, (b) NiO nanoslice, (c) NiO nanoparticle synthesized via Sol-Gel method and (d) the comparison of CV graph of three different shaped NiO at 50 mV/s [2].

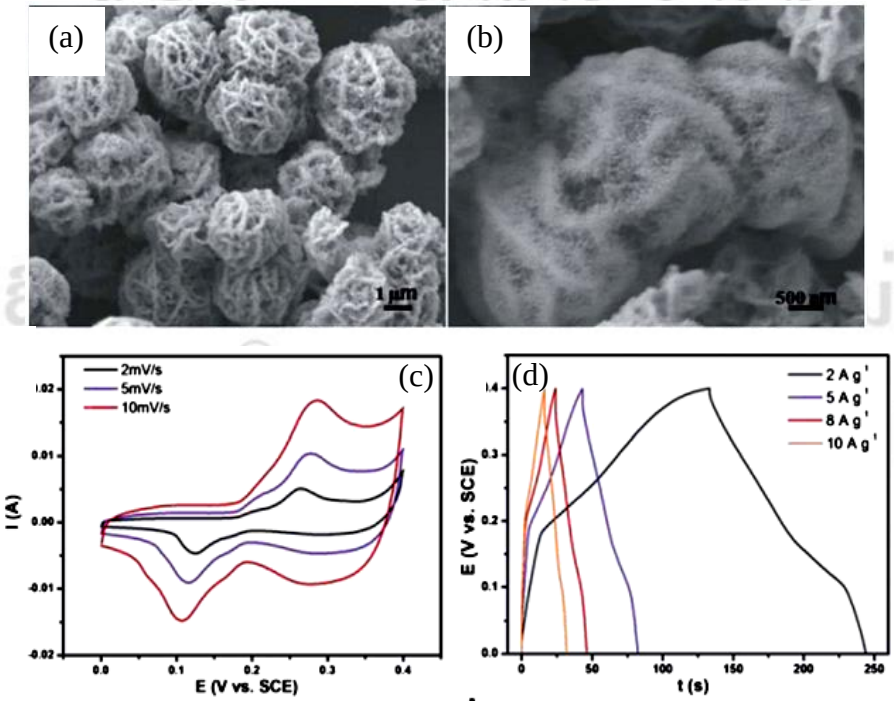

Figure 2.24 (a)-(b) the SEM pictures at low and high magnification, (c) CV curves at different scan rates and (d) GCD curves at various current densities of NiO network-like hierarchical microspheres by ultrathin nanowires self-assembly electrode [137].

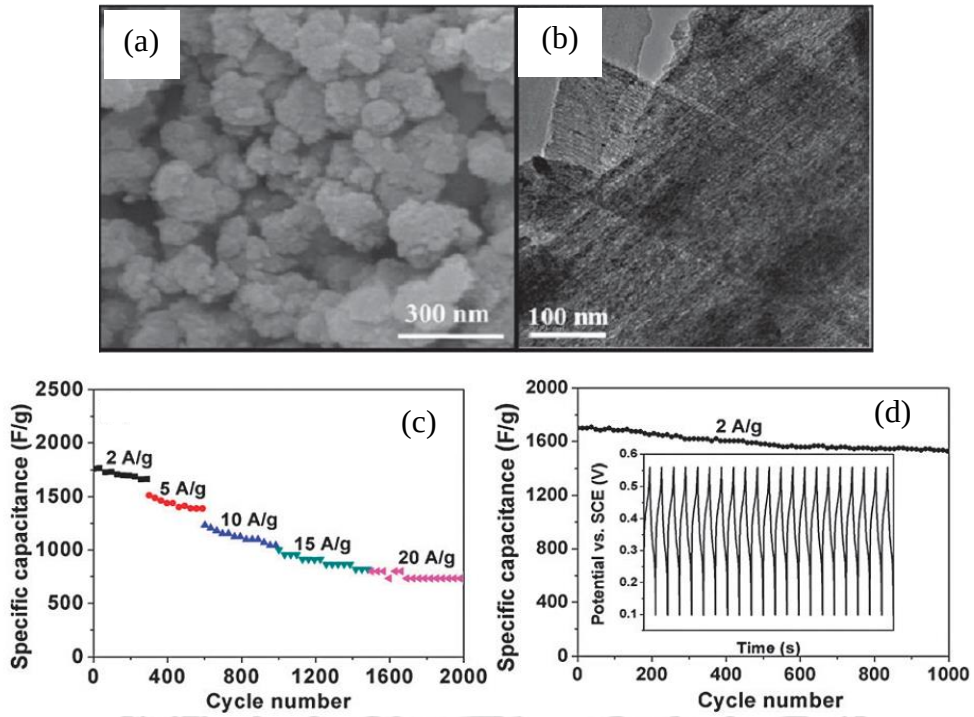

Figure 2.25 (a) SEM image, (b) High-resolution TEM image, (c) the specific capacitance retention at different current densities and (d) cycle performance at the current density of 2 A g^{-1} of the mesoporous NiO electrode [138].

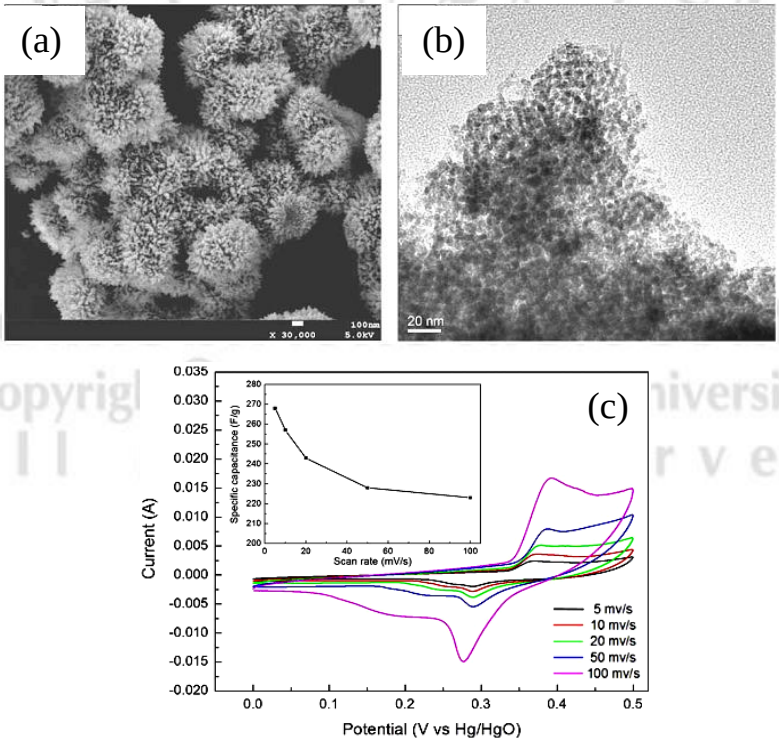

Figure 2.26 (a) SEM image, (b) high-resolution TEM image and (c) CV graph at various scan rate of the NiO with mesoporous structure, prepared by the template method [139].

-Hydrothermal Method: NiO hierarchical microspheres were prepared by direct thermal decomposition of $Ni(OH)_2$, synthesized via hydrothermal method in the air [137]. It is demonstrated that the NiO network-like hierarchical microspheres had a specific capacitance of 555 $F \cdot g^{-1}$ at 2 $A \cdot g^{-1}$, and 390 $F \cdot g^{-1}$ at 10 $A \cdot g^{-1}$ (Figure 2.24). Moreover, the slit-structured NiO were produced through a hydrothermal method by using the sodium dodecyl benzene sulfonate as an additive [138] (Figure 2.25). The NiO samples showed the specific capacitance of higher than 1700 $F \cdot g^{-1}$ at the window potential from 0.10 to 0.56 V at 2 $A \cdot g^{-1}$, and good cycle performance of 90% capacitance retention after 1000 cycles [138].

-Template Method: the NiO with mesoporous structure was prepared by a mixed surfactant template during the synthesis of mesoporous nickel oxide via hydrothermal precipitation method. The results showed that the as-prepared mesoporous NiO sample had a specific capacitance of 268 $F \cdot g^{-1}$ [139] as seen in Figure 2.26.

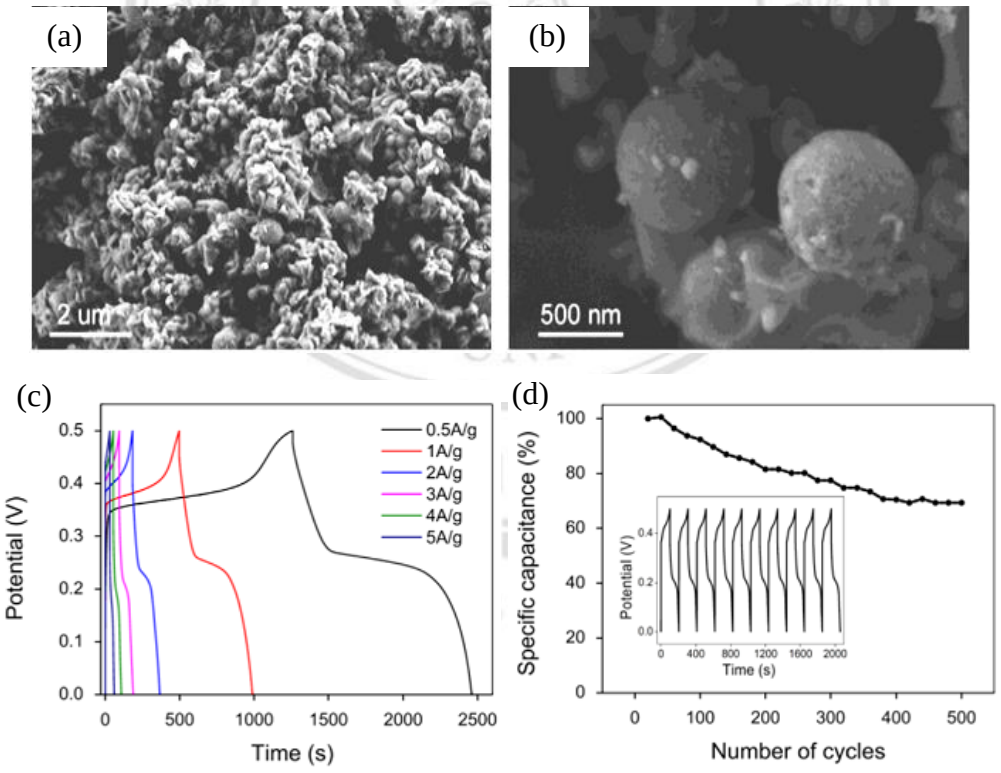

Figure 2.27 (a)-(b) SEM image at low and high magnifications, (c) GCD graph at various current densities and (d) the cycling capabilities at a current density of 3 A g^{-1} (The inset depicted the first 10 cycle of the test.) of the NiO of the nanospherical porous NiO electrode [140].

Furthermore, the porous carbon nanospheres were used as a hard template for producing a nanospherical porous NiO electrode. It was shown that the electrode had the high specific capacitance of 1201 $F \cdot g^{-1}$ at a current density of 0.5 $A \cdot g^{-1}$ and cycling performance of 70% capacity retention after 500 cycles [140]. The morphology and the electrochemical results were illustrated in Figure 2.27.

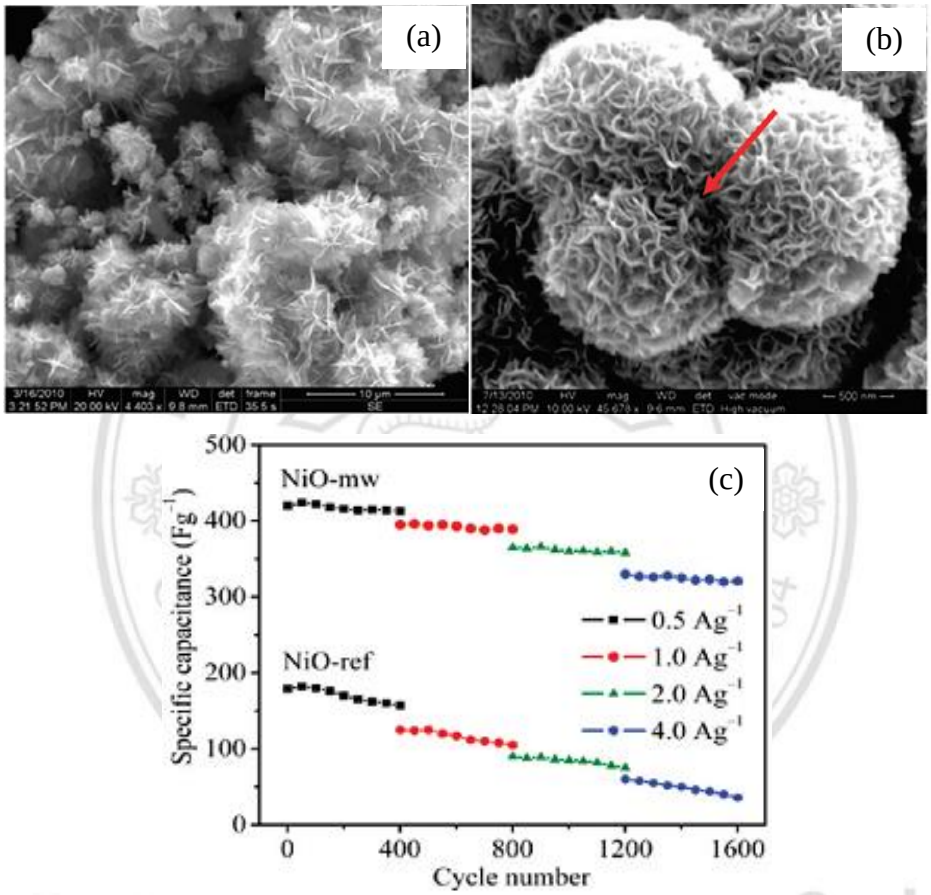

Figure 2.28 (a) SEM image of NiO prepared by reflux approach (NiO-ref), (b) SEM image of NiO prepared by microwave assisted heating technique (NiO-mw), (c) the comparison of GCD plot at various current densities vs cycle number of NiO-ref and NiO-mw electrode [141].

Microwave Assisted Heating Technique: this technique could prepare a hierarchical porous ball like NiO under homogeneous precipitation conditions [141]. The electrochemical results showed that the NiO synthesized by microwave method (NiO-mw) had a higher specific capacitance (370 F g^{-1} at a current density of 2 A g^{-1}) than the NiO prepared via the reflux approach (NiO-ref; 101 F g^{-1}) [141]. In Figure 2.28, it was observed that the NiO-ref sample (Figure 2.28 (a)) showed agglomerated flower like regular morphology randomly arranged nanoflakes. The NiO-mw depicted the

flower and rippled surface porous ball-like structure (Figure 2.28 (b)). The better electrochemical performance due to the rippled-shaped surface of NiO-mw could help the OH^- ions diffusion easier during the redox reaction [141]. The specific capacitance was revealed in Figure 2.28 (c).

Cobalt Oxide (Co_3O_4)

Co_3O_4 is a p-type semiconductor. It has the theoretical specific capacitance of about 3560 F g^{-1} and has cycle stability and corrosion resistance better than the NiO [142, 143]. The charge storage mechanism of the Co_3O_4 can be expressed as follows [142];

$$Co_3O_4 + OH^- + H_2O \longleftrightarrow 3CoOOH + e^- \quad (2.23)$$

$$CoOOH + OH^- \longleftrightarrow CoO_2 + H_2O + e^- \quad (2.24)$$

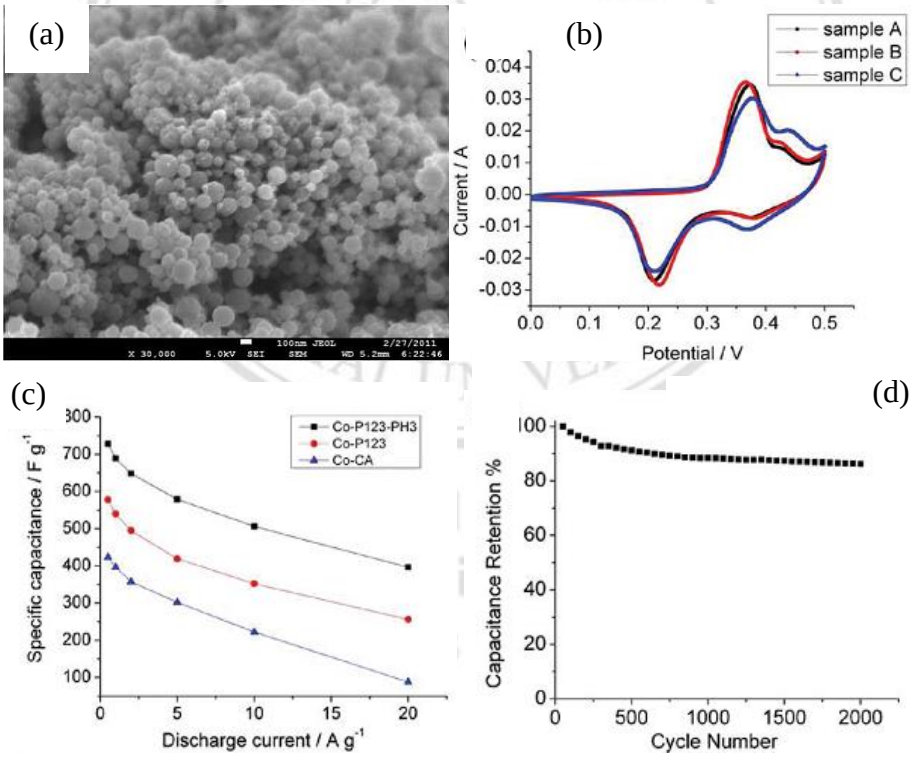

Figure 2.29 (a) SEM image of ultrafine Co_3O_4, (b) CV patterns of samples A=Co-P123-PH3, B=Co-P123 and C=Co-CA at the scan rate of 5 mV s^{-1}, (c) the specific capacitance vs. current densities and (d) the relationship between the average specific capacitance and cycling number of Co-P123-PH3 at 20 mV s^{-1} [144].

The hierarchically porous Co_3O_4 electrode was fabricated by cathodic electrodeposition through the liquid crystalline template. It had an excellent specific capacitance of 443 $F \cdot g^{-1}$ at 2 $A \cdot g^{-1}$ and 334 $F \cdot g^{-1}$ at 40 $A \cdot g^{-1}$. Additionally, it showed superb cycle performance with the specific capacitance maintains about 94.3% of the maximum value [145]. Mesoporous Co_3O_4 microspheres with crater-like structure were synthesized by using the mesoporous silica (MCM-41) as a template. This electrode presented a specific capacitance of 102 $F \cdot g^{-1}$ and the specific retention of ~74% after 500 cycles at a scan rate of 3 $mV \cdot s^{-1}$ [146].

3.1.4) Conducting polymer for pseudocapacitors electrode

Interestingly, conducting polymers provide a low cost, high conductivity, lightweight, flexibility, high specific energy and power when compare with other pseudocapacitive materials [147-149]. Various polymers are most studied for use as pseudocapacitors electrode such as polypropylene (PPy), polythiophene (PTh), polyaniline (PANi), polypyrrole, polyphenylene vinylene, poly (3,4-ethylene dioxythiophene) (PEDOT) and so on. Some structures of conducting polymers are shown in Figure 2.30.

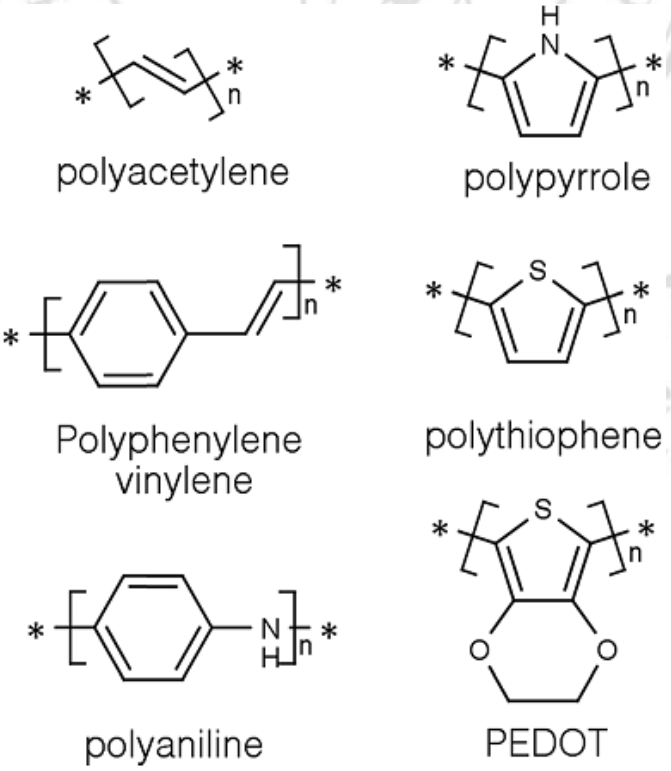

Figure 2.30 Various structures of conducting polymers [149].

Due to the conducting polymer storage charge via redox activity, it has higher specific capacitance than carbonaceous materials. The conductivity of conducting polymer was relied on the dopant level with the range of 1 to 10^3 S cm^{-1}) [150]. This value much higher than the conductivity of transition metal oxide, resulting in the superb power performance. The conducting polymers (Cp) can be either p-doped (anions; A^-) in the oxidation process or n-doped (cations; C^+) in the reduction process as shown in equation (2.25) and (2.26)

$$\text{(p-doped);}\ Cp + nA^- \longleftrightarrow Cp^{n+}(A^-)_n + ne^- \tag{2.25}$$

$$\text{(n-doped);}\ Cp + ne^- + nC^+ \longleftrightarrow Cp^{n-}(C^+)_n \tag{2.26}$$

During the charge/discharge process, the doping/undoping process was occurred by the insertion/extraction of counter electrolyte ions in the polymer backbones [151]. Table 2.3 summarized conductivity of different polymers [74].

Table 2.3. Summarized the synthesis method and electrochemical performance of some polymer (PPy, PT and PANi) based on pseudocapacitor electrode [152].

Materials	**Preparation method**	**Electrolyte**	**Maximum Specific capacitance**	**Cycle stability**	**Maximum energy density and corresponding power density**	**Ref.**
PPy	in-situ polymerization	2 M NaCl	325 F g^{-1}@ 0.6 mA cm^{-2}	63% after 500 cycles	26.7 Wh k g^{-1} @140.5 W kg^{-1}	[153]
	chemical oxidation	1 M KCl	576 F g-1 @0.2 A g^{-1}	82% after 1000 cycle	-	[154]
PTh	electro-polymerization	H_2SO_4-PVA gel	1357.31 mF g^{-1}	97% after 3000 cycle	23.11 mWh cm^{-2} @90.44 mW cm^{-2}	[155]
PANi	interfacial polymerization	1 M H_2SO_4	554 F g-1 @1A g^{-1}	10% after 1000 cycle	-	[156]

2.2 Batteries [157]

Batteries are classified using rate of discharging, energy density and cycle life, which was described above. They store chemical energy and convert into the electricity when needed. It is found that the rechargeable batteries are practical choices because they can keep/release the energy several times cycle. The well-known rechargeable batteries are lead-acid (Pb-acid), nickel-cadmium (Ni-Cd), nickel-metal hydride (Ni-MH) and lithium-ion (Li-ion) battery. The comparison of the energy densities, volumetric and gravimetric of various rechargeable batteries are shown in Figure 2.31. It is seen that the Pb-acid battery has the lowest energy density, followed the Ni-MH and Li-ion polymer battery have intermediate energy densities. The Li-ion battery has the highest energy densities. So, the Li-ion battery is the most required cells for energy storage and apply [157].

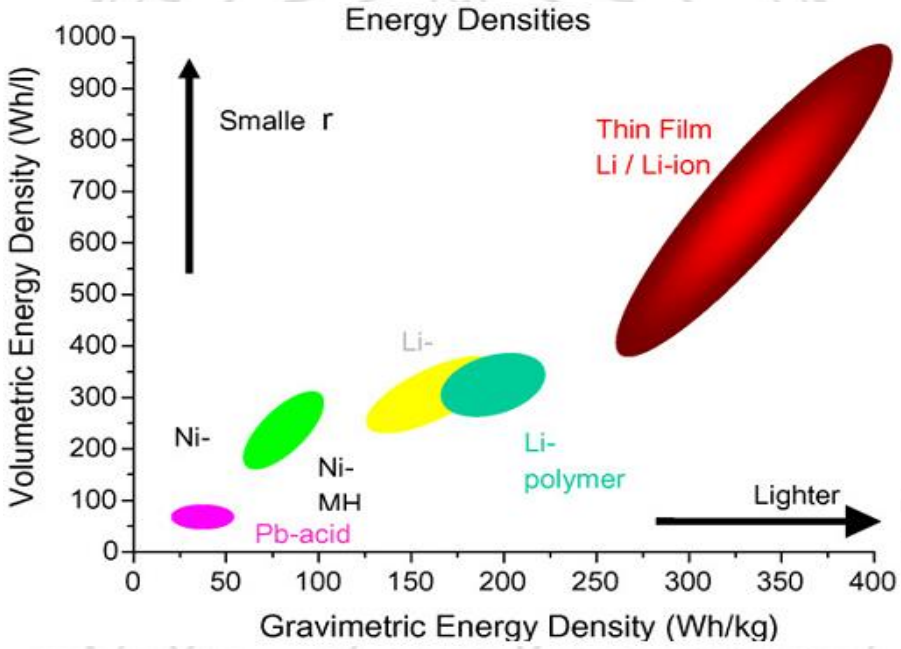

Figure 2.31 The schematic illustration of the comparison of the volumetric and gravimetric energy densities of various batteries [158].

2.2.1 Lead-acid (Pb-acid) Battery

Almost of the electric vehicles built in 1890-1910 used the Pb-acid batteries (energy density of ~10 Wh kg^{-1}). The Pb-acid batteries had applied in motor vehicles, telephone stations and train lighting [157]. The chemical reactions of this battery operate ~2.04V, which can be showed as follow;

$$\text{Anode; } Pb \longrightarrow Pb^{2+} + 2e^{-} \quad (2.27)$$

$$Pb^{2+} + SO_4^{2+} \longrightarrow PbSO_4 \quad (2.28)$$

$$\text{Cahoode; } PbO_2 + 4H^{+} + 2e^{-} \longrightarrow Pb^{2+} + 2H_2O \quad (2.29)$$

$$Pb^{2+} + SO_4^{2+} \longrightarrow PbSO_4 \quad (2.30)$$

$$\text{Overall; } Pb + PbO_2 + 2H_2SO_4 \xleftrightarrow{Charge/discharge} 2PbSO_4 + 2H_2O \quad (2.31)$$

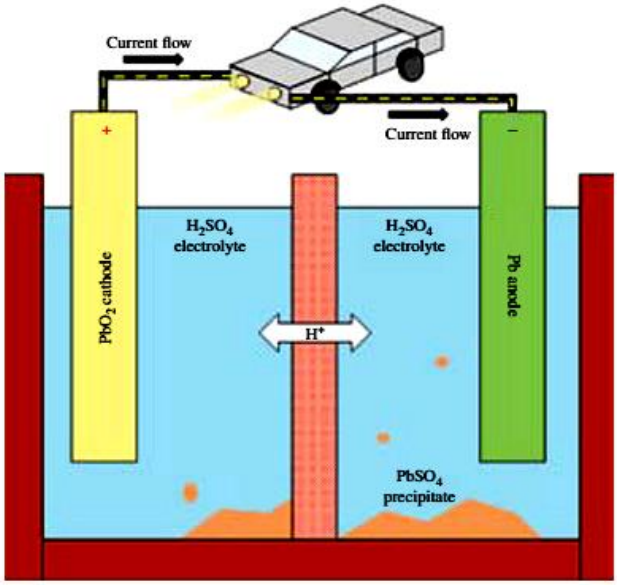

Figure 2.32 The Pb-acid battery working mechanism [158]

Figure 2.32 shows that the Pb-acid battery contains a current collector (Pb), spongy Pb anode, PbO_2 cathode and H_2SO_4 electrolyte. The Pb and PbO_2 has a low resistivity, which is 10^{-5} Ω·cm and 10^{-4} Ω·cm, respectively. While, the $PbSO_4$ (10^{8} Ω·cm), which is the product from the positive and negative electrode is an insulator. The $PbSO_4$ poorly solute in water, thus when the amount of $PbSO_4$ increase in the system, it needs to be added water into the battery for keeping the system working [157]. This show the limitations of the Pb-acid battery. Today, the Pb-acid batteries are built in sizes of <1 to >3000 Ah, the energy density ~25-35 $Wh \cdot kg^{-1}$, the power density ~70-100 $W \cdot kg^{-1}$ and the lifetime ~250-750 cycles.

2.2.2 Nickel-Cadmium (Ni-Cd) Battery [157]

During around the turn of the century, Edison and Junger developed the Ni-Cd batteries and available with “sealed” Ni-Cd cells in the 1940s. The Ni-Cd batteries employ in a wide range application such as portable tools, photography equipment,

military, instruments, and aerospace equipment [157]. The battery has a voltage of 1.25 V. The chemical reactions can be expressed in equation 2.32-2.34:

$$\text{Cathode; } 2NiOOH + 2H_2O + 2e^- \longrightarrow 2Ni(OH)_2 + 2OH^- \quad (2.32)$$

$$\text{Anode; } Cd + 2OH^- \longrightarrow Cd(OH)_2 + 2e^- \quad (2.33)$$

$$\text{Overall; } 2NiOOH + Cd + 2H_2O \longleftrightarrow 2Ni(OH)_2 + Cd(OH)_2 \quad (2.34)$$

Commonly, the Ni-Cd batteries consist of three main components such as the positive electrode, the negative electrode and the electrolyte, which is the nickel species, the cadmium species and the alkali electrolyte (KOH), respectively [157, 159]. The package of Ni-Cd batteries can be divided into button, cylindrical and prismatic cell. In the commercial, it usually finds the prismatic and cylindrical as shown in Figure 2.33.

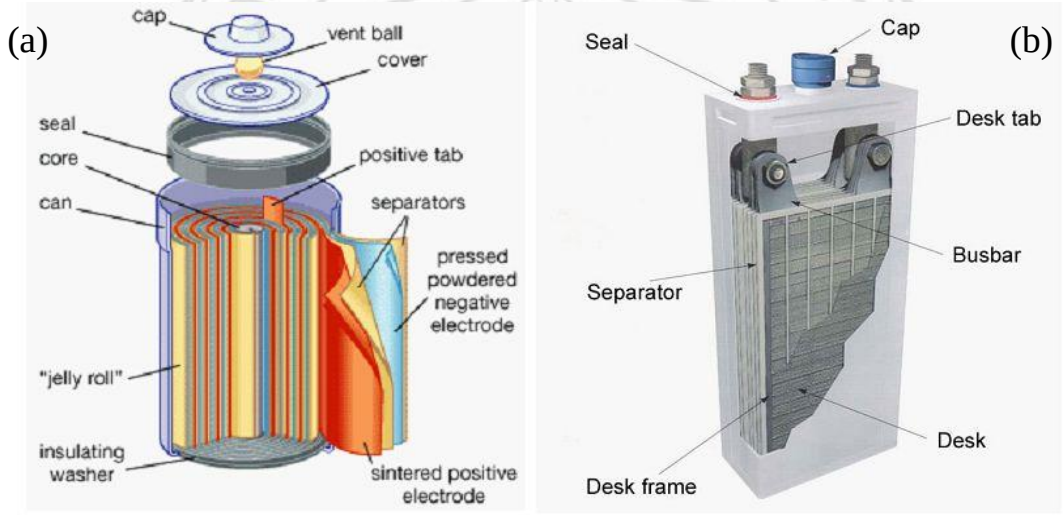

Figure 2.33 The construction of Ni-Cd battery (a) the cylindrical cell and (b) the prismatic cell [159].

Depending on the construction of the Ni-Cd batteries, they have the capacities in the range of 10 mAh to 20 Ah, energy densities of 40-60 Wh kg^{-1} and cycle life more than hundreds to thousands of cycles for sealed cells and vented cells, respectively [159]. However, it is found that cadmium is not only expensive but the construction of the cells has a higher cost than the Pb-acid batteries. Moreover, their limitation about the toxicity of cadmium is the main problem of this batteries. Due to the low maintenance and good reliability, the Ni-Cd batteries are still used in various applications, for example, emergency lighting, hedge trimmers, engine starting, electric shavers and aircraft [159].

2.2.3 Nickel-Metal Hydride (Ni-MH) Battery [157, 159]

In the 1990s, the Ni-MH batteries had been launched out in a commercial by the reason of replacing the Ni-Cd batteries in portable electronics because the Ni-MH batteries have a smaller size, higher performance and more environmentally friendly than the Ni-Cd batteries [159]. They consist of the positive electrode, which is nickel oxyhydroxide (NiOOH), the negative electrode, which is a metal hydride, consisting vanadium (V), nickel (Ni), titanium (Ti), etc. and electrolyte, which is alkali electrolyte (KOH). The chemical reactions of the Ni-MH batteries are illustrated as followed;

$$\text{Cathode; } NiOOH + H_2O + e^- \longrightarrow Ni(OH)_2 + OH^- \quad (2.35)$$

$$\text{Anode; } MH + OH^- \longrightarrow M + H_2O + e^- \quad (2.36)$$

$$\text{Overall; } NiOOH + MH \xleftrightarrow{charge/discharge} Ni(OH)_2 + M \quad (2.37)$$

In equation (2.35-2.36) on the cathode, the NiOOH is reduced to the $Ni(OH)_2$, which it has common two phases known as α-$Ni(OH)_2$ and β-$Ni(OH)_2$. While on the anode, the MH is dehydrogenated to metal (M) and H^+. The H^+ is oxidized and bonded with OH^-, formed H_2O [157]. This battery has Nominal cell ~1.2 V (<1.5 V), power density of ~200 W kg^{-1}, energy density about 60-120 Wh kg^{-1} [160] and high cycle life over 1000 cycles. The construction of Ni-Mh battery is depicted in Figure 2.34.

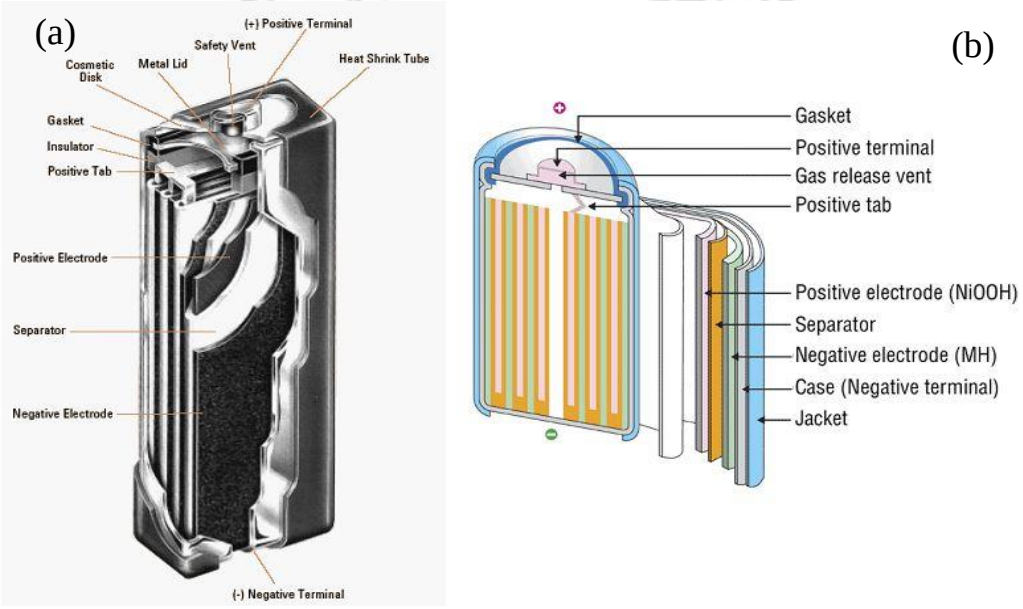

Figure 2.34 The construction of Ni-Mh battery (a) the prismatic cell and (b) the cylindrical cell [159].

However, the Ni-MH batteries have a high self-discharge up to 4-5% per day because of the dissolving of hydrogen in the electrolyte, which reacts with the positive electrode [159]. It is found that these batteries are applied in toothbrushes, electric razors, camcorders, mobile phones, medical tools and so on.

2.3 Sparking method [35-40, 161]

A sparking method is an alternative approach, employed to fabricate the thick/thin films and nanoparticles of transition metal oxide. This process is an inexpensive, well-controlled thickness and practical. The nanoparticles and porous films were synthesized via the supplying of high voltage arcing between two sharp metal tips under the atmospheric pressure. The nucleation mechanism can use to explain the formation of the obtained samples as shown in Figure 2.35.

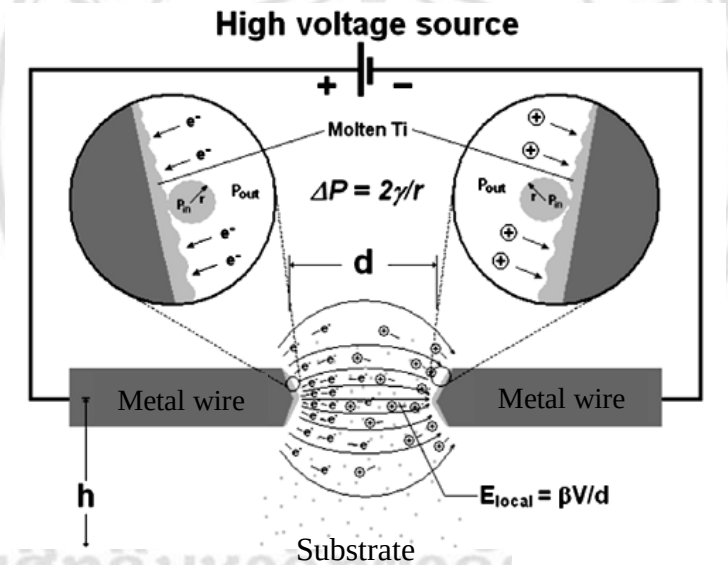

Figure 2.35 The nucleation mechanism of the sparked products such as transition metal oxide thick/thin films or nanoparticles [37].

In Figure 2.35, it is seen that the metal nanodroplets are created and deposited onto the substrate and then these products are oxidized in the air, formed transition metal oxide nanoparticles or films. This is because of the increasing of temperature and pressure at the surface of two metal tips, resulting from the bombardment of electrons and ions (ionization process) during the sparking operation [37]. The size of nanoparticle can be explained by using the Young-Laplace equation as shown in equation (2.34) [162].

$$\Delta P = \frac{2\gamma}{r} \tag{2.34}$$

Here ΔP is the difference of pressure between the inner (P_{in}) and outer (P_{out}) of nanodroplet, γ is the surface free energy of the molten metal and r is the radius of curvature [37, 39].

In addition, this method can be controlled the average particle size by adjusting the local electric field (E_{local}), which is applied across the metal tips as illustrated in equation (2.35)

$$E_{local} = \frac{\beta V}{d} \tag{2.35}$$

Here E_{local}, β,V and d is the local electric field, the field enhancement factor, applied voltage source and distance between the two metal tips, respectively [39, 163].

2.4 Characterization techniques

2.4.1 Interactions of electrons with the specimens [164]

The different details that are achievable by various techniques are come from the multitude of signals, arising when an incident electrons beam interact with a solid sample [165]. Several interactions can generate, as illustrated in Figure 2.36.

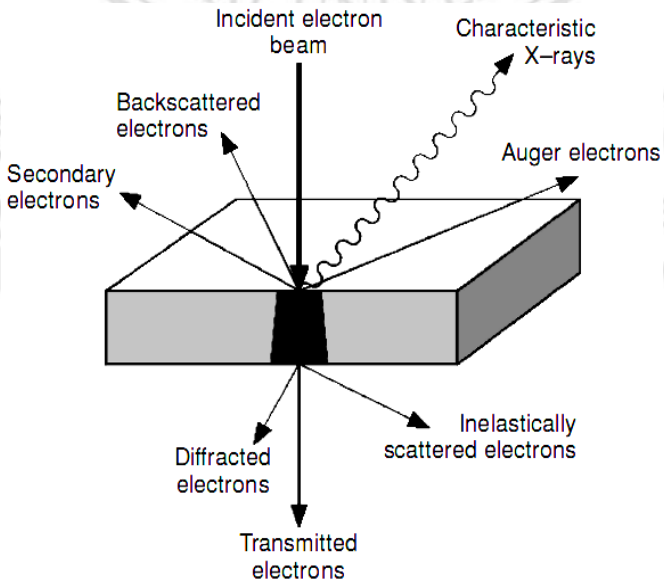

Figure 2.36 Various interactions of an incident electron beam with a solid material [164].

In Figure 2.36, the characteristic X-rays were generated when the enough energy of the incident electron beam knocks the electrons at the inner shells of atoms, followed the higher-energy electrons substitute to the lower vacated states.

Partial electrons elastically scattered in the backward path, known as the backscattered electrons. It is noted that the amount of electron relies on the average atomic mass as well as the local inclination of the specimens, related to the incident electron beam.

Secondary electrons are the outcome of the inelastic scattering of electrons in the conduction band of the samples (incident or backscattered electrons). These electrons will be ejected out the specimen when they achieve the sufficient energy.

Auger electrons come from a process similar to the creation of characteristic X-rays, however, when a higher-energy electrons fall into an empty states, the released energy will eject electrons at the outer shell rather than generate the characteristic X-ray.

For thin enough sample, some of the electrons will go through the specimen, occurring a transmitted electron beam, which contains the electrons from the incident beam. This elecron will not interact or have lost energy, resulting from the inelastic scattering processes. The lattice planes of the specimen have satisfied particular angular relations with the diffracted beam of electrons.

1) Backscattered Electrons (BSEs) [166]

The BSEs, which are investigated by SEM detector give details about composition and topographic data. With the energy of electron beam greater than 50 eV, BSEs (single or multiple scattering) are ejected from the surface. The elastic interaction between an electron and the atomic nucleus of specimen leading to the electron backscattered with the wide-angle directional change (~10-50% of the beam electrons) and the average energy retain ~60-80% of their initial energy. The elements with higher atomic numbers have more electrons are backscattered, resulting to higher backscattered signal. Thus, the yield of BSEs defined as the percentage of incident electrons, which are reemitted at the sample. By the use of the BSEs signal in the SEM characterization, it illustrates the atomic number contrast images. To illustrate, the BSEs yield is about 6% and 50% for the lighter (e.g. carbon) and heavier (e.g. gold) atomic number element, respectively.

The BSEs have large energy, avoiding them from the absorption by the specimen. The region, which BSEs are generated is noticeably larger than the secondary electrons, leading to the BSE image has inferior (lateral resolution ~1.0 μm. It is worse than a secondary electron image, which is around 10 nm. However, the BSEs has a large width of escape depth, so, it provides the details about features, which is deep beneath the surface. Moreover, it can be used to examine a good topographical image, which differs from image of secondary electrons, for example, some BSEs are blocked by area of the sample, thus, it creates a good contrast (black/white) image. Whereas the secondary electrons can give the signal around that area, so, it can not produce the contrast image.

2) Secondary Electrons [166]

The interaction between the primary electron beam and the solid specimen sample can produce the secondary electron signal. The atom is ionized by the primary beam. Then the electrons, which have loosely bound may be ejected, denoted as secondary electrons. Because they have a low energy about 3-5 eV, thus, they can only eject from a few nanometers region at the surface of materials. It is noted that the secondary electrons provide a high-resolution topographic information, which can explore depth to the surface sample in the order of 10 nm or more. The topographical image relies on how amount of the secondary electrons reach to the detector. Using low voltage incident electrons can produce secondary electrons from near surface of the sample, which can give more details morphology on the surface.

3) Characteristic X-rays [166]

The characteristic X-rays are generated when an electron at the inner shell is displaced by the impaction of the primary electron. An electron at the outer shell move down into the inner shell to rebalance its orbitals by the emission of an x-ray photon, following the ionized atom are back to the ground state. The characterization by using the characteristic x-rays provide the details about the chemical composition, which are widely utilized in microanalysis. Moreover, it is found that the characteristic x-ray peaks have a continuous background is produced via the deceleration of high-energy electrons, interaction with the nuclei of atoms and the electron cloud of the specimen. This signal is defined to the continuum x-ray or Bremsstrahlung signal. it holds the details, which is important to understanding and quantification of the emitted

spectrum, notwithstanding it is a background noise, which is generally removed from the spectrumbefore characterized.

4) Auger Electrons [166]

The relaxation of ionized atom is giving an Auger electrons. Again, the atom is ionized by the incident electron beam, leaving a hole in an inner shell. Due to the electron energy is unstable, the higher shell electron fills back and emit the excess energy. This energy is transferred to a further electron, which may receive sufficient energy to eject out of the specimen, known as the Auger electron, which has a characteristic energy. It can be employed to provide the chemical information. Because of their low energies, the Auger electrons are emitted only from the outer surface with the escape depth approximately a few nanometers, thus it is primarily utilized in surface analysis.

5) Transmitted Electrons [166]

The primary electrons move pass through the thin specimen (< 1 μm), generating the transmitted electron. Similar with the secondary and BSE detectors, the transmitted electron detector contains the scintillator, light pipe, and a photomultiplier. However, the detector is placed under the specimen, which is perpendicular to the optical axis of the microscope. Transmitted electrons can provide the information about elemental compositions and high-resolution images. It can be integrated the scanning electron beam to the transmission electron detector in order to get a scanning transmission electron microscopy.

6) Inelastic scattering [166]

Inelastic scattering refers to the process, which is the primary electron is lost energy, ΔE . In the electron microscopes, ΔE need to be substantially more than 0-1 eV before it is detected. The energy can be lost in various interaction process, to illustrate, it is transferred to atoms or electrons of the sample, leading to the different signals e.g. secondary electrons, X-rays, Auger, transmitted electrons and so on. These signal are utilized by the approaches of both elemental analysis and electron microscopy.

2.4.2 Structural characterization techniques

1) Scanning electron microscopy (SEM) [164, 166]

The SEM is very beneficial tool for the investigating of the surface of the materials due to it provides a better resolution than the optical microscope.

Generally, the electron beam source uses the tungsten (W) or Lanthanum hexaboride (LaB6), which is thermionic emitters as the filament in the visualization process. Resistive heating of the filament by a current to get a temperature in the range of 2000-2700 K results in the emission of thermionic electrons. The electron gun produces the electrons and accelerates these electrons to achieve the energy in the range of 0.1 – 30 keV towards the specimen [167]. The components of SEM illustrate in Figure 2.37.

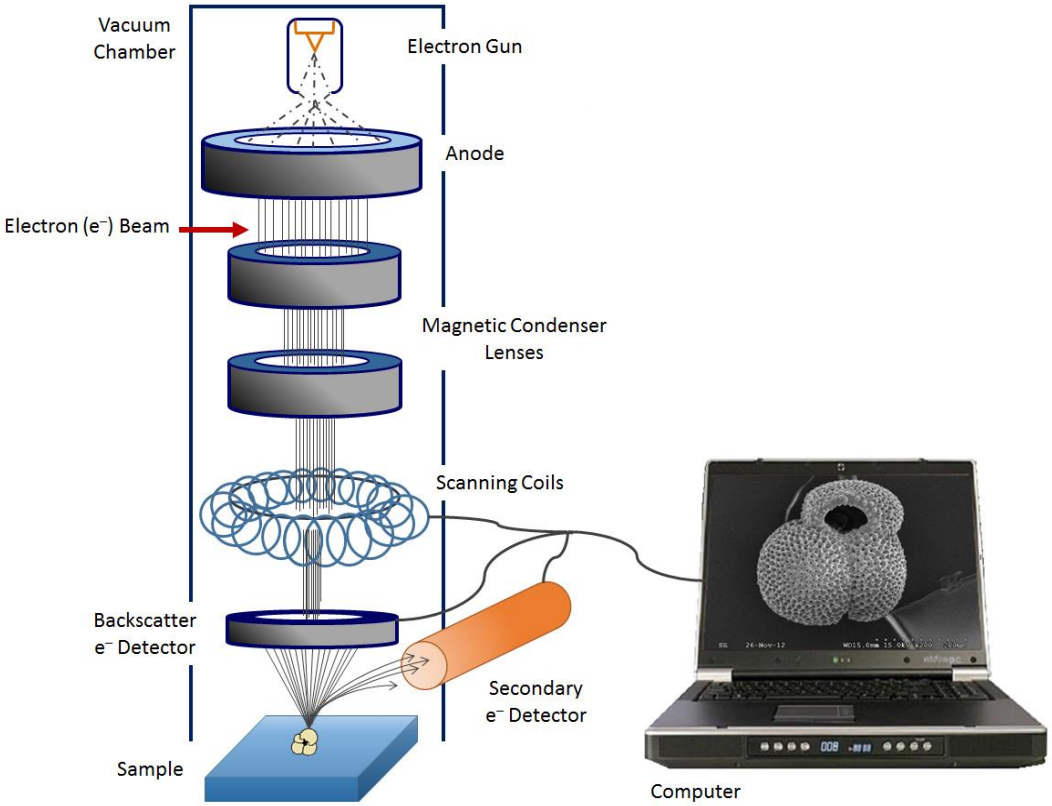

Figure 2.37 The main components of a scanning electron microscope [168].

A group of lenses uses to focus the electron beam on to the sample, interacting with the sample in a depth of ~ 1 μm. Again, when the electron beam hit on the sample, various signals are created and these signals can be used in the imaging processing. Two signals are frequently used are secondary electrons and BSEs. Simultaneously, the generated signals are recorded, and an image formed pixel by pixel. The details about morphology, surface topology and composition can be obtained. For field emission

scanning electron microscope (FESEM), it provides a less electrostatically distorted image and clearer the resolutions with a spatial resolution below 1 nm (~6-fold better) and, compared with the convention SEM. Thus, the FESEM can give the topographical and elemental details at the magnifications of 10x to 300,000x.

The X-ray photon is also recorded by the adjustment detector. This signal is extensively used for the compositional composition examination, which known as energy-dispersive X-ray (EDX) analysis. The samples for the SEM and EDX characterization are limited to a solid and non-volatile.

2) Transmission electron microscopy (TEM) [164]

Similar the principle of the optical microscope but the difference in the uses of electrons sources not photons. Thus, the TEM provide a very high resolution because the wavelength of electrons is around 0.03 Å, in contrast, the photons have the wavelength more than 1000 Å. TEM is a microscopy technique, which uses a beam of electrons transmitted through an ultra thin sample. When electron travels through the thin sample, these signal is magnified and focused onto an imaging device e.g. a fluorescent screen, a layer of photographic film, and the detection of a sensor (CCD camera).

It is noted that the scattered or diffracted electrons signal, which is glanced away from the axis of optical microscope can be blocked by using an aperture. Hence, the transmitted electron beam can create a contrast on the fluorescent screen, relying on its different intensity. The density or thickness of the specimen has mostly effect to the intensity. In the crystalline structures, it is observed that the behavior of electron beam generally diffracts rather than absorbs. The intensity of the diffraction depends on the plane orientation in the structure, which is related to the electron beam. It provides the different scattering pattern of the electrons with an angular distribution, known as the diffraction patterns. The components of the TEM are shown in Figure 2.38.

As mention above in Figure 2.38 shows that the electrons have numerous interaction with the sample, through the bottom side. The transmitted beam has passed through the specimen with no interaction. The diffracted beams contain electrons, which have not lost energy (elastically scattered) but have satisfied angular criteria (similar to Bragg's law for X-rays) and have been scattered into a new path. The transmitted and

diffracted beams can be used to generate images of the specimen with a very high resolution (on the order of 1 nm). Additionally, the diffracted electrons can be create selected area diffraction pattern, which gives a crystallographic information.

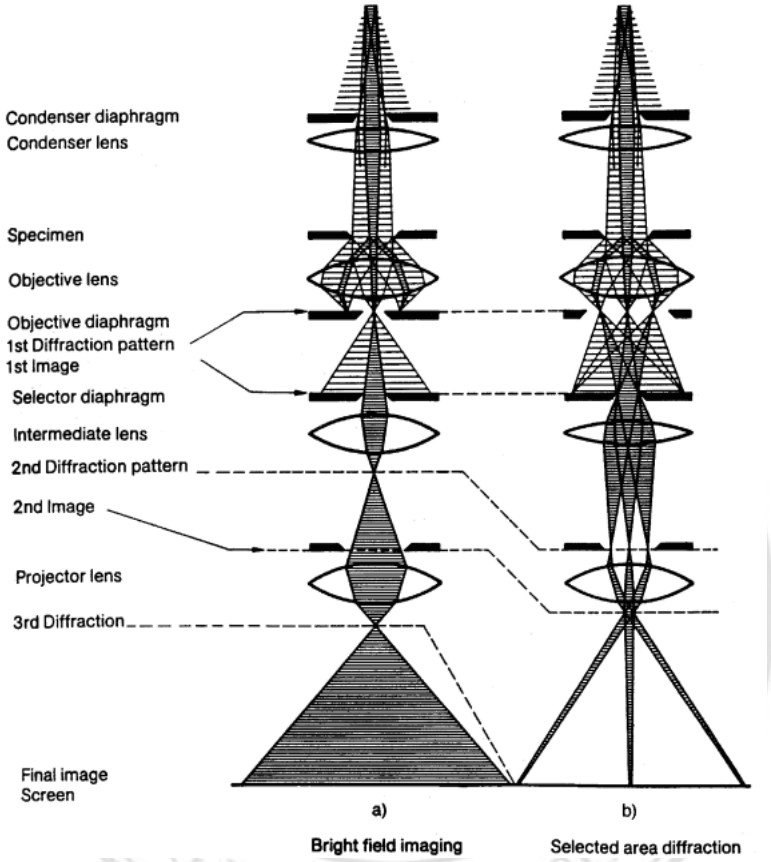

Figure 2.38 (a) Bright field imaging mode, (b) Selected area diffraction mode.

3) X-ray Diffraction (XRD) Techniques [169]

The XRD is used to determine the corresponding atoms within a crystal structure. An X-rays beam strikes to sample and scatters in varying directions. The XRD is a constructive interference between monochromatic X-rays and a crystalline specimen. The cathode ray tube is generally used as the X-rays source. These X-rays are filtered and generated the monochromatic radiation. After that, they are collimated to concentrate and directly hit onto the sample. X-rays, which are scattered from a crystalline sample can productively interfere, creating a diffracted beam. these interferences can be considered by the Bragg's Law.

As seen in Figure 2.39, the two parallel planes $A-A'$ and $B-B'$ have the same Miller indices (h, k, l), divided by the interplanar spacing (d_{hkl}). It is assumed that the X-ray beams, which are parallel, monochromatic, and coherent beam with the wavelength

λ are incident on these two planes of the specimen at the angle of θ. The two rays of this beam, named 1 and 2, are scattered by atoms P and Q. Afer that the interference of

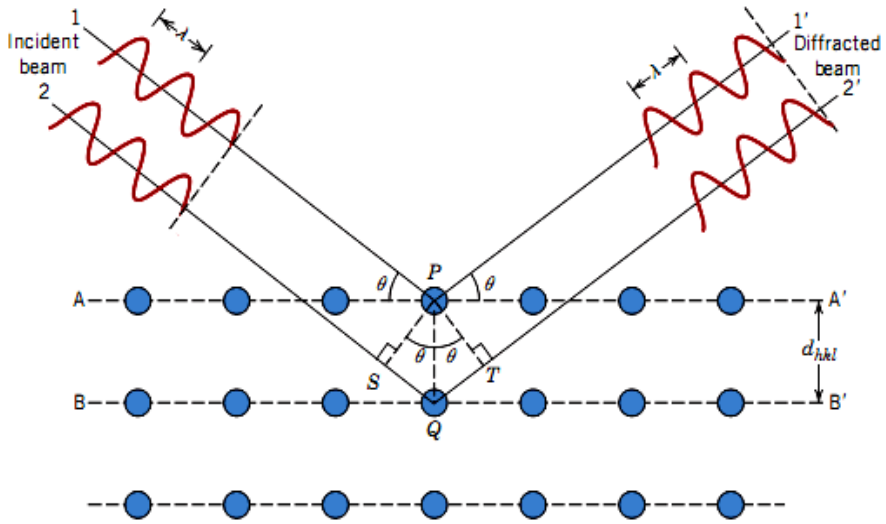

Figure 2.39 The diffraction of X-rays by planes of atoms ($A-A'$ and $B-B'$).

the scattered rays $1'$ and $2'$ occur with the angle of θ to the planes. If the path If the path length difference between the rays of $1-P-1'$ and $2-Q-2'$, which is $\overline{SQ}+\overline{QT}$ is equal to the wavelengths (integer number, n). Thus, from Bragg's Law equations it can illustrate as below;

$$n\lambda = \overline{SQ} + \overline{QT} = 2d_{hkl}\sin\theta \tag{2.36}$$

Where n is the order of diffraction (any integer i.e. 1,2,3,...n), which should not greater than unity. Thus, it can be simple express, corresponding to the x-ray wavelength as well as the lattice planar spacing to the angle of the diffracted beam. If Bragg's law is not related, resulting in the interference yield will not be generated (low intensity diffracted beam). Moreover, it is found the magnitude of the distance between two parallel planes, especially the interplanar spacing (d_{hkl}) related with the Miller indices (h, k, and l), and the lattice parameters. Generally, this technique are widely utilized to examine the crystalline nature and crystal structure of wide ranging samples.

3) X-Ray Photoelectron Spectroscopy (XPS)

The XPS is a high surface sensitive analysis, which is broadly used for investigating of the oxidation state as well as the compositions of the samples. This

technique also knows as the Electron Spectroscopy for Chemical Analysis (ESCA) because it provides precise quantitative details of the surface of the materials.

Based on technique also know as the Electron Spectroscopy for Chemical Analysis (ESCA) because it provides precise quantitative details of the surface of the materials. Based on the photoelectric effect, a monochromatic characteristic X-rays with a fixed energy ($h\nu$) incident toward a sample, it will be absorbed by the atoms and then the secondary electrons will be ionized with the kinetic energy (E_k). Besides, two main energy components should be considered are the binding energy (E_b) and work function (Φ), which are the required energy to move the electron up to the Fermi level and to raise the electron from the Fermi level to the vacuum level, respectively. The over all relation can be expressed in equation (2.37)

$$E_k = h\nu - (E_b + \Phi) \tag{2.37}$$

In other word, the binding energy of the photoelectron can be given by

$$E_b = h\nu - (E_k + \Phi) \tag{2.38}$$

Using fixed photons and if E_k and Φ of the samples are measured, thus, it can be calculated the binding energy of the electron. This energy is a characteristic of atoms, which can be used to identify the different elements of the samples. The XPS signals are recorded in the series of peaks from the electrons emission, which interact with the surface, lacking the inelastic collisions. It is known that high intensity of such electrons reduces significantly with the distance, so, XPS can provide only the details beneath a certain distance, especially from the surface, indicating termed as surface sensitive analysis.

The binding energy of an electron also depends on the oxidation state as well as the local chemical variation, which is showed by a small shift in the peak positions of the XPS result, called as chemical shifts. A Schematic diagram representing of 2p photoelectron of copper is shown in Figure 2.40.

The XPS peaks results are named by using the quantum numbers, which indicate the levels of the electron creation. It is consist of a principal quantum number (n), an

orbital quantum number (l) and spin quantum number (s). Thus, it is expressed as nl_{l+s}. Materials with nonzero orbital quantum number (l >0), the spin moment is coupled with

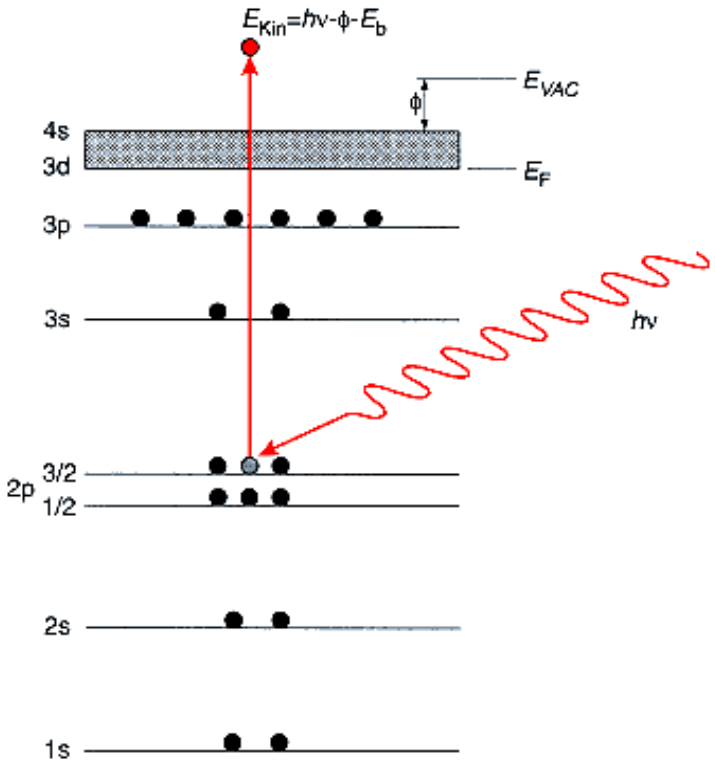

Figure 2.40 A Schematic diagram representing of 2p photoelectron of copper.

orbital moment (called as l-s coupling) and it has a total momentum (j), which can be showed as followed;

$$j = l \pm s = l \pm \frac{1}{2} \tag{2.39}$$

It is known the each state can fill with $2j+1$ electrons. Hence, almost XPS peaks usually represent in doublets and the intensity ratio of the component is $\frac{l+1}{l}$.

5) Raman Spectroscopy [170]

Raman spectroscopy is the measurement of the wavelength and intensity of inelastically scattering of monochromatic light, usually from a laser in the visible, near infrared and near ultraviolet range, from molecules. The laser can be used as the excitation source. In conventional Raman spectroscopy, visible lasers are used (e.g., Ar^+, Kr^+, Nd: YAG, He-Ne, diode) to stimulate the molecules to high energy "Virtual" states of excitation. A Raman photon is emitted if a molecule undergoes a

transition to a higher vibrational energy state than its original state (Stokes Raman scattering), a lower energy vibrational state (Anti-Stokes Raman scattering) and the original state (Rayleigh scattering) which shown in Figure 2.41. Normally, Stokes Raman scattering has the higher intensity. Raman scattering can be used to elucidate the structure of molecules and crystals.

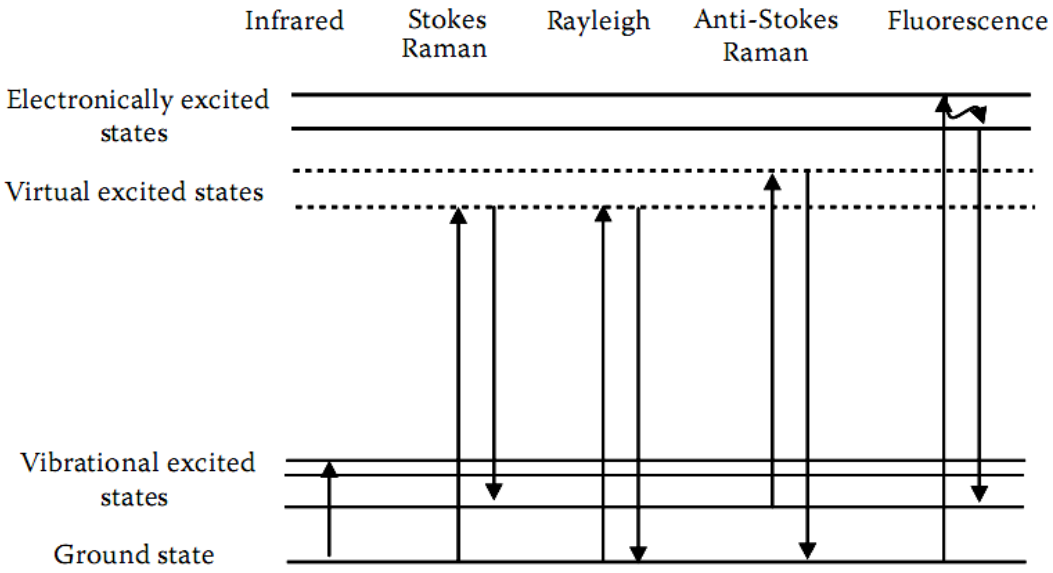

Figure 2.41 Energy diagram of light-induced excitation [170].

6) Ultraviolet-visible (UV-vis) spectroscopy

Energy is absorbed in the UV or visible region because of a change in the electronic excitation of the molecule, resulting in a corresponding change in its ability to absorb light in the UV-visible region of the electromagnetic radiation. This is the main leading to the color transition. The relationship between energy absorbed in an electronic transition and the frequency (υ), wavelength (λ) and wave number (Ψ) of radiation producing the transition is given as:

$$\Delta E = h\upsilon = h\frac{c}{\lambda} = h\Psi c \qquad (2.40)$$

Where h = Planck's constant, c = the velocity of light and ΔE = Energy absorbed in an electronic transition in a molecule from the ground state (lower energy) to excited state (higher energy). The energy absorbed relies on the energy difference between ground state and excited state. For example, the material with a smaller difference has larger the wavelength of absorption. Base on the principal, the characteristics of an

absorption band are the position and intensity. The position of an absorption band relates to the wavelength of radiation, which energy is equal to the amount of energy required for an electronic transition. In the case of the intensity of absorption, it depends on two factors: Firstly, the probability of interaction between the radiation energy and the electronic system. Secondly, the difference between the ground state and excited states. The intensity of absorption is achieved from Beer-Lambert's law [171]:

$$A = \varepsilon cl = -\log \frac{I}{I_0} \tag{2.41}$$

Where A = the measured absorbance, ε = the absorptivity, l = the path length of the cell and c = the concentration of the analyte, I_0 = the incident intensity and I = the transmitted intensity. The light absorbed by the sample in a cuvette is shown in Figure 2.42.

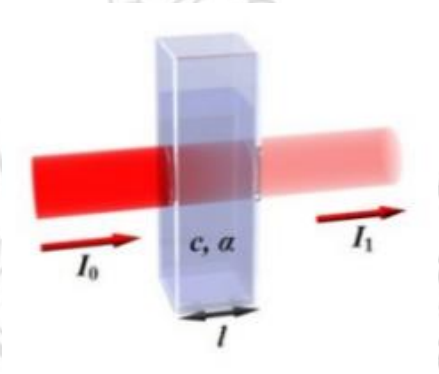

Figure 2.42 Light absorbed by the sample in a cuvette [172].

In Figure 2.42 and the Lambert' s law, it is seen that the amount of light absorbed is varying proportionally to not only the concentration (c) but the distance/thickness of the absorbing layer, known as the part length of light (l)

Considering the definition of the transmittance (T) is the ratio of the primary incident intensity and the transmitted light intensity. Again, the intensity of transmittance can gain from Beer-Lambert's law, which is expressed below [171];

$$T = \frac{I}{I_0} = e^{-\alpha t} \tag{2.42}$$

Where α is absorption coefficient, which can be calculated, from equation (2.42), and t is the film thickness

$$\ln T = -\alpha t \ln e \tag{2.43}$$

$$\alpha = -\frac{\ln T}{t} \tag{2.44}$$

Moreover, the α can be obtained by using the measured absorbance from equation (2.41) and (2.24)

$$-\log\left(\frac{I}{I_0}\right) = -\alpha t \log e \tag{2.45}$$

$$\alpha = -\frac{2.3026\,A}{t} \tag{2.46}$$

UV-Vis Spectroscopy is a powerful tool for the characterization of semiconductor samples. Optical absorption characteristic of semiconductor nanoparticles can be explained by the principle of excitation of the valence shell electrons to the conduction band, creating an electron-hole pair in the system. The semiconductor nanoparticles display a size quantization effects, dependence of the change in the band gap energy (ΔE_g) in the semiconductor nanoparticles on their size radius (R) of a spherical particle can be expressed as:

$$\Delta E_g = h^2\pi^2\left(\frac{1}{m_e} + \frac{1}{m_h}\right)\frac{1}{R^2} - \frac{1.8e^2}{\varepsilon}\cdot\frac{1}{R} \tag{2.47}$$

Where m_e and m_h correspond to the effective mass of electron and hole respectively, ε is the dielectric constant of the semiconductor material. The decreasing in particle size can shifts the absorption edge from the infrared to the visible region of the electromagnetic spectrum as the band gap energy of the semiconductor increases.

Furthermore, the band gap energy value can be achieved by using the Tauc relation, which is shown by equation (2.48);

$$\alpha h\nu = A(h\nu - E_g)^n \tag{2.48}$$

Where hν is photon energy and A is a constant. To estimate the band gap energy, the plot of $(\alpha h\nu)^{1/n}$ vs. the hν is plotted. The extrapolation of the linear portion to the X-axis (photon energy axis) provides the band gap energy. The n value relies on the electronic transition category. n value can be 1/2, 2, 3 and 3/2 for direct allowed transition, indirect allowed transition, direct forbidden transition and indirect forbidden transition, respectively.

7) Atomic force microscope (AFM)

The AFM is employed to examine the surface topology of the materials in the 3D direction (x, y as well as z direction) with a wide-ranging scale size from angstroms to 100 um. It is equipped with a sharp tip (probe), which is placed at the end of a microscale cantilever. The silicon or silicon nitride are generally used to fabricate tip. The radius of curvature is in the order of nanometers. To fabricate the image of the surface topology of the samples, the tip is attracted or repelled onto proximity of the surface. The forces between the tip and the specimen rely on Hooke's law. The bending of the cantilever is detected by the laser, which is reflected onto the split photodiode. A piezoelectric ceramic, which is a tube scanner is used to control the transition of the tip or the specimen. The scanner has the resolution in sub-angstrom level, which can move in the direction of x, y or z. The z direction is perpendicular to the sample, known as height. The relation between the laser deflection vs. a location of the tip give details about the hills and valley, which create the topography of the surface and explain about the features as well as the shape of the materials. Because of this technique utilizes the force of interaction of the atoms on the tip, the AFM technique can examine the non-conducting samples.

Generally, AFM analysis can be performed in two modes such as contact and tapping (non-contact) modes. The AFM contact mode is the most widely used technique. This mode has the tip close contact with the surface of the sample during the scanning. The result of contact mode provides the 3D image with the nondestructive analysis. Tapping mode is better for characterization and imaging of the soft samples. The tip is oscillated at its resonating frequency and located over the sample, thus, the tip contacts the sample only for a short time. The basic working diagram of the AFM is shown in Figure 2.43.

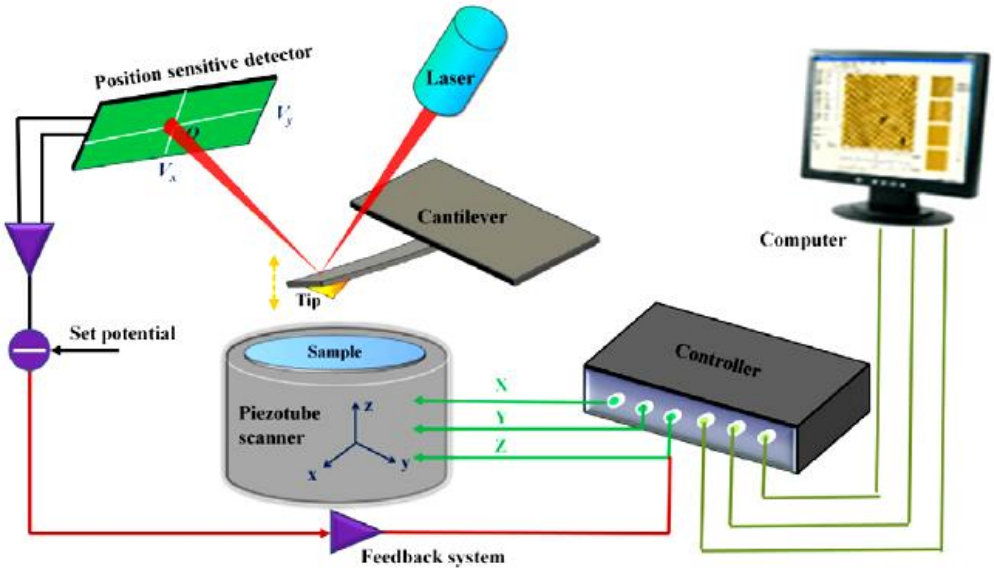

Figure 2.43 The basic working diagram of the AFM [173].

8) Nitrogen physisorption [174]

Nitrogen adsorption/desorption are operated at 77 K. it is broadly used to analyze and estimate the specific surface areas and pore volumes of samples. The adsorption arises between the solid surface and the gas, called as adsorbent and adsorbate, respectively. The nitrogen isotherm illustrates the varying of adsorbed gas volume at a fixed temperature vs. the pressure. The results represent the various shape, which provides direct details about the character of adsorbent and adsorbate interaction, for example, monolayer/multilayer formation, pore structure (size, shape as well as connectivity), pore filling and pore emptying and layer-by-layer adsorption. It is usually known that the mesoporous materials have the adsorption, which is controlled by multilayer formation and capillary condensation/evaporation. While the micropore structure is dominated by stronger interactions. According to the IUPAC classification [174], the porous materials can be categorized into six isotherm types, is showed in Figure 2.44.

The type I is obtained, attributing to microporous solids, where the uptake is limited to micropore accessibility.

Type II shows the typical unrestricted monolayer-multilayer adsorption for non-porous or macroporous adsorbents.

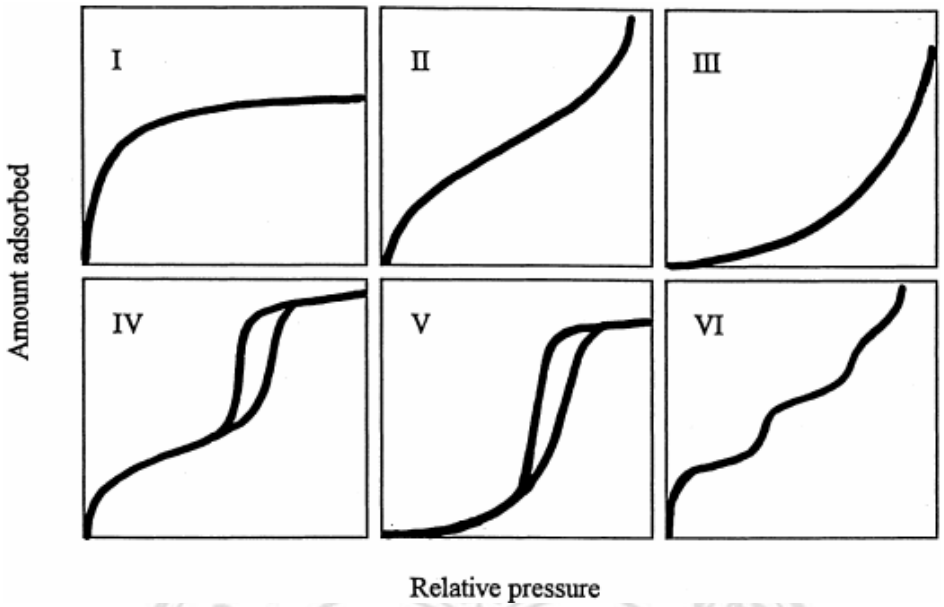

Figure 2.44 The IUPAC classification of adsorption isotherms [175].

Type III; this type is not common; relating to the adsorbent-adsorbate interactions are rather weak such as the characteristic nitrogen adsorption on polyethylene/ the typical of adsorption of water vapor on the clean graphite.

Type IV; the data represents the hysteresis loop, controlled by the capillary condensation. The initial region of the graph can be resulting to monolayer-multilayer adsorption like the result in type II. This characteristic is found in various mesoporous materials.

Type V; it shows the capillary condensation and hysteresis but it differs from type IV. Due to the initial region is related to the type III, demonstrating. the adsorbent-adsorbate interactions are weak

Type VI is related to multi-step layer-on-layer adsorption on a uniform, non-porous surface and non-polar adsorption materials. The sharpness of the steps relies on the homogeneity of the adsorptive, the adsorbent surface, and the temperature.

8.1) Adsorption isotherm analysis

The adsorption isotherms are determined for surface area and porosity measurement. The data are treated for estimating the surface area by using the Brunauer-Emmett-Teller (BET) and for determining the pore size distribution by using Barrett, Joyner & Halenda (BJH) method, as showed below.

- BET method [176]

BET method is the most generally employed for the surface area analysis of the materials. The BET equation is shown as followed;

$$\frac{1}{V_a\left[\left(P/P_0\right)-1\right]} = \frac{\left(C-1\right)}{V_m C}\left(\frac{P}{P_0}\right) + \frac{1}{V_m C} \tag{2.49}$$

Where V_a = the volume adsorbed, V_m= the monolayer volume, P/P_0 = the relative pressure, C = the BET constant, the $\frac{(C-1)}{V_m C}$ and the $\frac{1}{V_m C}$ value are the intercept and slope, which are identified from the BET linear plot, as represented in Figure 2.45.

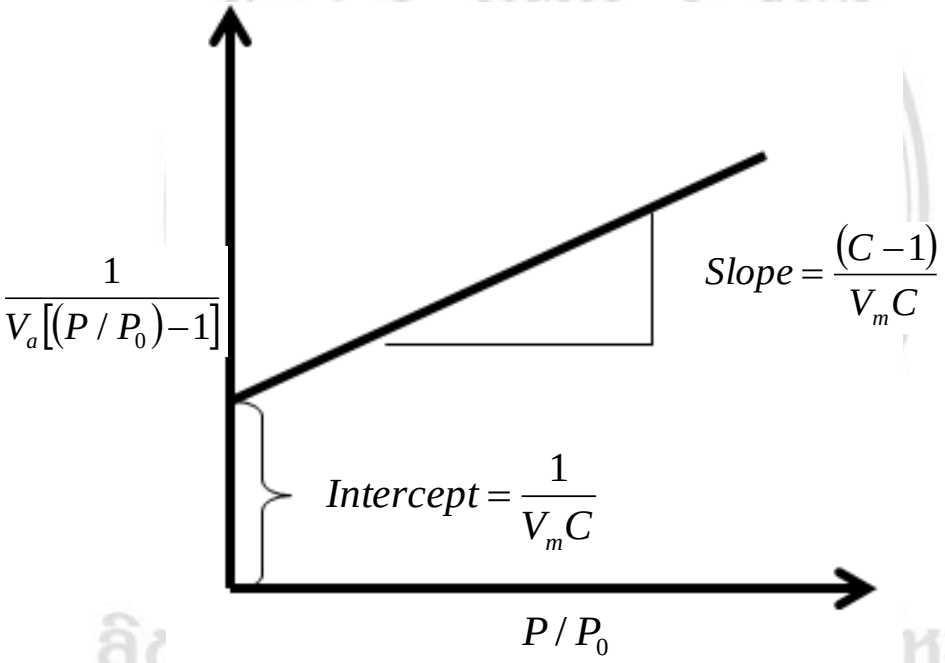

Figure 2.45 BET plot displays a linear feature [177].

From the obtained results, V_m and BET constant can be easily calculated. Thus, the specific surface area (A) in the unit of $m^2 g^{-1}$ is estimated by the equation 2.50.

$$A = n_m a_m N_a \tag{2.50}$$

Where n_m, a_m and N_a are the mole of adsorbate per gram of adsorbent, the effective cross-sectional area of one adsorbate molecule and Avogadro constant (6.022×10^{23} mol^{-1}), respectively. If V_m in milliliters at the standard temperature and pressure (STP), the equation can be illustrated below;

$$A = \frac{V_m}{22414} a_m N_a \tag{2.50}$$

Where 22414 is the volume occupied by one mole of the adsorbate gas at STP, in the unit of milliliters. The a_m value for N_2 at 77K is 0.162 nm^2 for Ar at 87 K is 0.143 nm^2. Moreover, for the BET plot, a minimum of three points data is required.

- BJH method [178]

BJH method is the most usually used for determining the mesopore size distribution. It is based on the Kelvin equation and modified for the multilayer adsorption by utilizing the statistical film thickness, as shown in equation (2.51)

$$r_p = r_k + t \tag{2.51}$$

Where r_p is the pore radius, which is the results from the Kelvin radius (r_k) plus the statistical film thickness (t). The t value is estimated from the standard isotherm (t-plot). The r_k can be determined from Kelvin equation, as revealed in equation (2.52)

$$r_k = \frac{-2\gamma V_L}{RT\ln(P/P_0)} \tag{2.52}$$

Here γ is the surface tension, V_L is the molar volume of the liquid adsorbate and R is the gas constant, (8.314 J mol^{-1} K^{-1}). For nitrogen adsorption, at 77 K the Kelvin equation can be expressed as followed

$$r_k = \frac{-4.14}{\log(P/P_0)} \tag{2.53}$$